MIXTURES OF CHARGED-NEUTRAL SUPERFLUIDS

A DISSERTATION SUBMITTED TO
THE GRADUATE SCHOOL OF ENGINEERING AND SCIENCE
OF BILKENT UNIVERSITY
IN PARTIAL FULFILLMENT OF THE REQUIREMENTS FOR
THE DEGREE OF
DOCTOR OF PHILOSOPHY
IN
PHYSICS

By
Fatmanur Ünal
December 2016

MIXTURES OF CHARGED-NEUTRAL SUPERFLUIDS
By Fatmanur Ünal
December 2016

We certify that we have read this dissertation and that in our opinion it is fully adequate, in scope and in quality, as a dissertation for the degree of Doctor of Philosophy.

Mehmet Özgür Oktel(Advisor)

Balázs Hetényi

Menderes Işkın

Bilal Tanatar

Ali Ulvi Yılmazer

Approved for the Graduate School of Engineering and Science:

Ezhan Karaşan
Director of the Graduate School

ABSTRACT

MIXTURES OF CHARGED-NEUTRAL SUPERFLUIDS

Fatmanur Ünal
Ph.D. in Physics
Advisor: Mehmet Özgür Oktel
December 2016

Motivated by the developments of artificial magnetic fields (AMFs) enabling coupling to the neutral particles of ultracold quantum gases, we have theoretically studied charged-neutral mixtures in various settings. The techniques that have been used to manufacture these AMFs are highly sensitive to the internal degrees of freedom of the atoms, resulting in unequal coupling to the components of a mixture. We demonstrate the possible consequences of this unequal coupling by considering two different systems. First, we examine an impurity problem in a fermion background under an AMF coupling selectively to the impurity in a ring trap. We calculate the response of the system exactly by using Bethe Ansatz and argue that the AMF can be employed as a probe to analyze polaron formation. Secondly, we explore Bardeen-Cooper-Schrieffer theory of superconductivity in the presence of a charge imbalance under an AMF. We analytically calculate the gap equation for any degree of asymmetry between the Landau level spectra of up and down spin particles, and show that the system displays reentrant superconductivity both in magnetic field and temperature. Apart from mixtures, we also investigate the non-equilibrium Hall response of a topological system. The strength of an AMF applied on a optical lattice can be suddenly changed without creating Eddy currents, allowing us to quench the system across a topological phase boundary. We report a fractional Hall response for the resulting non-equilibrium system and discuss possible implementations for cold atom experiments.

Keywords: Ultacold atoms, artificial gauge fields, Bethe Ansatz, polaron, BCS theory, high-field superconductivity, two-channel model, topological phases, Haldane model, non-equilibrium Hall response..

ÖZET

YÜKLÜ-YÜKSÜZ SÜPERAKIŞKAN KARIŞIMLAR

Fatmanur Ünal
Fizik, Doktora
Tez Danışmanı: Mehmet Özgür Oktel
Aralık 2016

Nötr parçacıklardan oluşan aşırı soğuk kuvantum gazlarına çiftlenebilen yapay manyetik alanların (YMA) geliştirilmesinden motivasyon alarak, bu tezde çeşitli koşullar altındaki yüklü-yüksüz karışımları teorik olarak inceledik. Bu YMA'ları üretmek için kullanılan teknikler, atomların iç serbestlik derecelerine karşı oldukça hassastır. Bu nedenle, Raman lazerle oluşturulan YMA'lar, bir karışımın bileşenleri ile eşit olmayan bir şekilde çiftlenirler. Bu eşit olmayan çiftlenmenin olası sonuçlarını iki farklı sistemi dikkate alarak gösterdik. Öncelikle, bir fermiyon denizindeki bir safsızlık problemini, saf olmayan atoma seçici olarak çiftlenen bir YMA altında inceledik. Bethe Ansatz'ı kullanarak sistemin kesin tepkisini hesaplayarak, YMA'nın polaron oluşumunu analiz etmek için bir sonda olarak kullanılabileceğini savunduk. İkinci olarak, YMA altındaki bir yük dengesizliğinin varlığında Bardeen-Cooper-Schrieffer süperiletkenlik teorisini inceledik. Yukari ve asağı dönel parçacıkların enerji spektrumu arasında bir asimetri olması durumunda, aralik denklemini analitik olarak hesaplayarak, sistemin hem manyetik alan hem de sıcaklıkta yeniden girişli süperiletkenlik gösterdiğini ispatladık. Yüklü-yüksüz karısımların yanı sıra, topolojik sistemlerin denge dışı Hall tepkilesini de araştırdık. Optik örgülere uygulanan YMA'ların Eddy akımlarına neden olmadan bir anda degiştirilebilir olması, sistemi topolojik bir faz geçişinin diğer tarafına aniden geçirmemize olanak sağladı. Ortaya çıkan denge-dışı durumundaki sistemin kesirli bir Hall tepkisi olacağını göstererek, soğuk atom deneyleri için olası uygulamaları inceledik.

Anahtar sözcükler: Aşırı soğuk atomlar, yapay ayar alanları, Bethe Ansatz, polaron, BCS teorisi, güçlü-manyetik-alan süperiletkenlik, iki-kanal modeli, topolojik fazlar, Haldane modeli, denge-dışı Hall tepkisi..

Acknowledgement

I would like to say that the last four years I have been working on this PhD thesis have been a great experience and satisfying in many ways. For this, I would like to express my heartfelt gratitude to my supervisor Mehmet Özgür Oktel for every second he spent helping me become an independent researcher and showing me how physics is done. I was lucky to have a second excellent advisor at Cornell University; I am deeply grateful to Erich Mueller who somehow always finds time to meet in his busy schedule. I have learned a lot from his clear way of thinking and his insight into cold atom experiments.

I would like to thank my thesis monitoring committee; Balázs Hetényi and Menderes Işkın for their insightful comments, not only at the end but also during the development of this thesis. I want to also thank Prof. Bilal Tanatar and Prof. Ali Ulvi Yılmazer for their time, reading and reviewing this thesis. I have also benefited a lot from the faculty members at Bilkent University through the numerous courses I have taken from them and the valuable discussions we had in the corridors. My groupmates at Bilkent and Cornell deserve special thanks for our most helpful discussions on physics. And I want to thank all my dearest friends at Bilkent and Cornell for our enjoyable time together.

I am happy to acknowledge financial support from The Scientific and Technological Research Council of Turkey (TÜBİTAK) which has funded me throughout my PhD study and during my visit to Cornell University; from Department of Physics for providing funding for my conference visits; from Erich Mueller for partially funding one of my conference visits; and finally I would like to thanks Laboratory of Atomic and Solid State Physics at Cornell University for hosting me.

Last but not least, all my love and thanks go to my family; my parents Sermin and Bilal; my sisters Zeynep, Hande and her husband Mehmet. They have never ceased to encourage and support me even when we were separated by an ocean.

Contents

1 Introduction **1**

2 Impurity under an Artificial Magnetic Field **8**

2.1 The Model 11

2.2 The Ansatz 13

2.2.1 $N = 2$ Particles 13

2.2.2 $N - 1$ Fermions, One Charged Particle 16

2.3 Solution of the BA Equation 18

2.3.1 Energy 22

2.3.2 Angular Momentum 24

2.3.3 Effective Mass 27

2.3.4 Correlations 30

3 Pairing in the Presence of Change-Imbalance **36**

3.1 The Model 39

3.1.1 Renormalization of the Two-Channel Hamiltonian 41

3.2 Gap Equation 43

3.3 Phase Diagram 45

4 Non-equilibrium Topological Response **51**

4.1 Single Dirac Cone 53

4.2 The Haldane Model 56

4.2.1 Infinite System 56

4.2.2 Beyond Linear Response 59

4.2.3 Strip geometry 61

4.3 Harmonic Trap 64

5 Conclusion **66**

A Publications in SCI journals **79**

List of Figures

1.1 Illustration of the dressed states of a system in $F = 1$ hyperfine level, representing the experimental scheme employed by Ref. [1]. The sublevels are first split by a real magnetic field (dotted lines for $m_F = \pm$), and then coupled with resonant Raman transitions $k_{1,2}$. Then a second, position-dependent Zeeman shift is applied (solid lines), creating a spatially changing detuning $\delta(r)$. So, the energy of the dressed states will change with position, and a particle adiabatically following such a dressed state will experience a geometric phase. 4

2.1 A simple illustration of the system. $N - 1$ uncharged fermions (light gray) and a single charged impurity (dark gray) are trapped on a ring. The impurity is interacting with the fermions via Delta-function interaction. An AMF couples exclusively to the impurity. The dynamics of the system depends on the interaction strength between particles and the total flux through the ring $\beta = \frac{qRA}{\hbar}$. ©2015 APS 10

2.2 Energy of the three lowest states vs. interaction strength for $N = 2$ particles, and zero total angular momentum. Only scattering states are displayed. Energy is calculated in three different ways. Lines are from Eq.2.19 direct analytical solution without employing BA, which is algebraically same as the two-particle BA calculation (Eq.2.18). Diamonds are from the general N-particle BA calculation (Eq.2.27). ©2015 APS 15

2.3 A representation of graphical solution to BA equation. The $\cot \pi k$ term in Eq.2.27 diverges at every integer k and there is a root between every consecutive integer independently from $\lambda(\beta)$. By changing the value of λ, all roots can be adjusted so that the total angular momentum constraint is satisfied. ©2015 APS 19

2.4 Ground state energy vs. flux β for $N = 2$ particles with total angular momentum n. Eigenstates for flux β with total angular momentum n are also eigenstates for flux $\beta + 1$ with total angular momentum $n+1$. The system can be analyzed by considering flux values between $-1/2 < \beta < 1/2$ for all n. As the flux is increased by one adiabatically, the system evolves to a higher excited state which has one more unit of total angular momentum. The crossings between different eigenstates is not a problem for adiabatic evolution since only states with different total angular momentum n are degenerate. ©2015 APS 20

2.5 Ground state energy vs. interaction strength for $N = 1000$ particles and zero total angular momentum. Numerical solution of BA equation Eq.2.27 (dots) are virtually indistinguishable from analytical solution (circles) $E =$(Fermi energy of $N-1$ fermions)$+\Delta E$. Error between the numerical and analytical solutions are too small to observe even in the regimes where the assumptions for analytical calculation fails. ©2015 APS 23

2.6 Angular momentum of the impurity vs. interaction strength for $N = 100$ particles for (a) attractive and (b) repulsive interactions from the analytic calculation; numerical solutions produce the same results. In the non-interacting limit, the impurity carries all the angular momentum $(n - \beta)$. L_1 saturates to zero for infinitely strong repulsive interactions as the total angular momentum is shared equally between all particles. The same behavior holds for excited states. For strongly attractive interactions, L_1 saturates to half the total value, signifying dimer formation with one background particle. The insets in both figures focus on the weak interaction limit. ©2015 APS 25

2.7 The angular momentum of the charged particle vs. flux at varying interaction strength for $N = 100$ particles. As expected L_1 depends linearly on flux. The slope of the line decreases with increasing interaction strength indicating higher values of effective mass of the impurity. ©2015 APS 26

2.8 Effective mass of the impurity vs. interaction strength for $N = 50$ particles and zero total angular momentum $n = 0$. (a) For attractive interactions, m^* saturates to twice the mass of the impurity due to the formation of a tightly bound pair. The inset shows the behavior around zero interaction in more detail. For attractive interactions, the effective mass (given by Eq.2.39) is almost insensitive to flux change. (b) For repulsive interactions, m^* converges to N. As flux β increases, this saturation gets faster. The dependence on the flux is more prominent for small particle numbers. ©2015 APS 27

2.9 Resonant behavior in m^* for β comparable to N. When the dragging effect of the background particles overcomes the driving force of the magnetic field, m^* can become negative. When the second derivative of the energy with respect to flux becomes zero, m^* diverges. This divergence does not alter the infinitely-strong interaction limit. ©2015 APS 28

2.10 Effective momentum density in k-space for different interaction strengths. In the strongly interacting limit, the distance between adjacent BA roots (wavevectors) is one. For small c, the roots are closer to each other around $(n - \beta)$, which means the impurity carrying $n - \beta$ units of angular momentum in the non-interacting limit first disturbs the fermions which are momentum matched to that value. ©2015 APS 29

2.11 Two-particle correlation function for $N = 2$ particles. As expected, g_{12} at zero separation decreases with increasing interaction strength. For weak interactions, the correlation function at zero decreases with increasing flux. However, for strong interactions, the correlation is almost insensitive to flux change due to the fermionization of the charged particle. ©2015 APS 31

2.12 Two-particle correlation function for $N = 50$ particles. (a) For weak interactions, Friedel oscillations occur as interference of two waves with wavelengths related to $k_F - \beta$ and $k_F + \beta$. (b) At strong interactions, the correlation becomes zero at zero separation since the impurity is effectively indistinguishable and g_{12} and the frequency of Friedel oscillations are almost insensitive to flux change. ©2015 APS 32

2.13 Kinetic energy of the particles vs. interaction strength for $\beta = 0.2$ and $\beta = 10.2$ for $N = 50$ particles. The inset shows the interaction potential contribution to the total energy. The initial increase in interaction energy follows the increase in the interaction strength. However, beyond a certain strength, the tendency of the fermions to avoid the impurity is more dominant. These plots are obtained by taking the derivative of the total energy with respect to c. Alternatively, the interaction potential energy is also obtained by using the two-particle correlation function at zero separation. Both results are plotted in the inset showing remarkable agreement. ©2015 APS 34

3.1 Superconducting phase diagram. For weak magnetic fields, semiclassical approximation predicts monotonically decreasing critical temperature T_C (dashed line). For strong magnetic fields, one must consider the Landau level structure. A fully quantum mechanical treatment shows oscillations in T_C at high magnetic fields, corresponding to peak in the density of states. 38

3.2 Phase diagram of the system as a function of dimensionless temperature $\tilde{T} = k_B T/\hbar\omega$ and effective density $n_1 = N\pi^2\ell^3$ where N is the real-space density and $\ell = \sqrt{\hbar/m\omega}$. Notice that increasing AMF, $B = m\omega/\sqrt{q_1 q_2}$, corresponds to lower n_1 values. Two frequency ratios $\omega_r = 1$ and $\omega_r = 0.95$ are displayed for the same interactions strength $\tilde{a}_s = a_s(N\pi^2)^{1/3} = 0.53$. For $\omega_r = 1$, there is SC transition at any field, the oscillations in T_C (stars) originates from the LL structure. For $\omega_r = 0.95$, this oscillation evolves into bubble SC regions (shaded areas). The system is not SC even at zero temperature between the bubbles and the transition becomes weakly reentrant in temperature. At the low (many LLs) and high field (only LLL) regimes, T_C is not affected significantly by a small charge imbalance. ©2016 APS 46

3.3 Pairing susceptibility (left panel) and respective phase diagrams (right panel) for three frequency ratios $\omega_r = 1, 0.95, 0.75$. The system is made dimensionless with effective magnetic energy $\hbar\omega$ as in Fig.3.2 and decreasing n_1 corresponds to increasing AMF at fixed real-space density N. The phase diagrams are in linear scale in order to cover $T_C = 0$ and plotted for intermediate field strengths where charge imbalance effects are most prominent. a) Pairing susceptibility of equal charges diverges at low temperature, guaranteeing SC for any field value. Divergence is more pronounced at LL thresholds. The corresponding phase diagram (b) is obtained by Eq.3.23. The phase boundary is also highlighted on the surface. c) Even a slight asymmetry between the charges, $\omega_r = 0.95$, lifts the low temperature divergences and the oscillations in (b) turn into bubble SC phases (d). Each LL susceptibility peak is split into smaller peaks, thus, the bubble phases branch into smaller bubbles for weaker interactions (not displayed). e,f) The mismatch between LL spectra is greater for smaller ω_r, resulting in prominent reentrance with temperature. The maximum reentrance temperature is controlled by $\hbar|\omega_1 - \omega_2|$. ©2016 APS 48

4.1 Non-equilibrium Hall conductivity, C_{neq}, of a single Dirac cone following a ramp of the gap from $-\Delta$ to Δ in time 2τ as shown in inset. C_{neq} is measured in units of e^2/h, and the product $\Delta\tau/\hbar$ is dimensionless. In the sudden quench limit ($\tau = 0$), $C_{neq} = 1/6$ and as $\Delta\tau \to \infty$, $C_{neq} \to 1/2$. The dashed line shows prediction of the LZ theory from Eq.(4.9). ©2016 APS 55

4.2 Haldane model. (a) illustrates the matrix elements of the tight-binding Hamiltonian in Eq.(4.10); hoppings $t_1, t_2 e^{\pm i\phi}$ and bias $2M$ between A (dark) and B (light) sublattices. (b) Phase diagram showing the Chern number of the lowest band $C = 0, \pm 1$. The arrow indicates the quench studied in the text. Bands touch at a single Dirac point for $M_C = \pm t_2 3\sqrt{3}\sin\phi$. ©2016 APS 57

4.3 Non-equilibrium Hall response of the Haldane model. The energy offset M is suddenly quenched from $M_i = M_C + \Delta M$ to $M_f = M_C - \Delta M$, where $M_C = t_2 3\sqrt{3}\sin\phi$ is the topological transition point. Here $\phi = 0.6\pi$ and $t_2 = 0.1t_1$. For small quenches one reaches the fractional regime in which $C_{neq} \to 2/3$. ©2016 APS . 58

4.4 Nonlinear Hall response $C_{neq} = \partial X/\partial I$ following a quench, for transverse displacement X resulting from an impulse I. The parameters are adimensionalized by using the unit length of the lattice. The system is quenched between states ΔM around the transition point M_C as detailed in the text. The Hall response of a non-equilibrium system saturates to equilibrium result ($C = 1$ in this case) for large impulse. Linear response regime shrinks for decreasing ΔM. ©2016 APS 60

4.5 Haldane strip with armchair termination, for parameters introduced in Fig.4.2(a). Unit cell is given by the shaded area. We label the layers in the finite y-direction. Green (thick vertical) lines represent how nearest- and next-nearest-neighbor hoppings are assigned into these layers to calculate the current density $\mathcal{J}_\ell$. ©2016 APS 62

4.6 Equilibrium Hall conductivity of the strip as a function of number of layers in the finite direction. The system is in CI state at $M = 0$ and $M = M_C - 0.1$, for $t_2 = 0.1t_1$ and $\phi = 0.6\pi$. Hall conductivity approaches to the quantized bulk value as $1/L$ for increasing strip width. ©2016 APS 63

4.7 Effect of a harmonic trap with $\hbar\omega = 0.09t_1$ in the finite direction for $M = 0$, $t_2 = 0.2t_1$ and $\phi = 0.5\pi$. (a) Local density of states along the finite direction where the center is a CI and the edges are metallic. The Fermi energy is indicated with the red line. (b) Current density flowing along the strip with (dark line) and without (light line) trap, in the absence of an electric field. The force exerted by the trap $F_y = -m\omega^2 y$ results in anomalous currents in the central topological region according to $j_x = eCF_y/h$ (dashed line). ©2016 APS 64

Chapter 1

Introduction

Since the first observation of a Bose-Einstein condensate using rubidium [2] and then sodium [3] atoms, the physics of ultracold atomic gases has advanced tremendously. These systems are essentially the quantum emulators of Feynman's original idea [4], where an isolated and controllable quantum system is used in simulating other quantum mechanical phenomena arising naturally in condensed matter. Rapid developments in experimental techniques, regarding cooling and probing, have rendered ultracold quantum gases the ideal laboratory to observe many-body physics. Several theoretical models have been observed for the first time in these systems such as the superfluid to Mott transition or the BEC-BCS crossover, and several others challenged by these experimental achievements [5, 6, 7, 8].

The main appeal of the ultracold atomic gases has been the level of control and tunability of the experiments. One can engineer the confining potentials into a desired geometry, choose particle types, create a clean system or add impurities at will, and tune the inter-particle interactions from infinitely-strong attractive to infinitely-strong repulsive limit. The dominant interaction between these atoms is through s-wave scattering which can be tuned via Feshbach resonances between the atoms [9]. On the other hand, the constituents of the cold atom experiments are neutral atoms. Hence, at the first glance, it may seem impossible to observe the effects originating from an external magnetic field. However, one can always

try working around this problem by *mimicking* the effect of a magnetic field in the system.

Under a magnetic field, a charged particle performs cyclotron motion and it is possible to create the effect of this Lorentz force artificially. Initial efforts in this direction employed rotation using the analogy with the Coriolis force. However, rotation as a synthetic magnetic field brings further constraints on the confining potential of the ultracold system to keep particles from escaping the harmonic trap at high frequencies and requires perfectly symmetric traps [10].

A recent development in ultracold quantum gases is the creation of geometrically induced artificial magnetic fields (AMFs) [11, 12]. This method does not impose any constraint on the symmetries of the underlying system and enables the investigation of orbital magnetism in a wide variety of settings. Classically, the fields (electric, magnetic) are the important quantities, not the potentials. Contrarily, the magnetic field enters into the Hamiltonian in the form of vector potential in quantum mechanics, enabling coupling even if the strength of the magnetic field vanishes at some point in space. When a charged particle moves along a closed loop, the effect of the magnetic field can be characterized in terms of the Aharonov-Bohm (AB) phase that the particle feels. This AB phase is given by the flux enclosed by the loop. In other words, it depends only on the geometry of the contour, not on the dynamics (e.g. the velocity) of the particle while traveling around the loop. One can generalize this concept and say that if a particle acquires a geometric phase over the course of a closed loop, it feels an effective magnetic field.

Light-induced AMFs exploit the relation between the AB phase of a real magnetic field and the Berry phase of an adiabatic cyclic evolution. Berry phase is a geometric phase which emerges when a particle adiabatically follows a local eigenstate while it moves along a closed contour in the parameter space of the Hamiltonian. We encounter the Berry phase in various systems throughout the condensed matter literature. In the case of the AB effect, the Hamiltonian

$$H = \frac{1}{2m}\Big(\vec{p} - \frac{qBx}{\hbar c}\hat{y}\Big)^2, \tag{1.1}$$

is position dependent and a charged particle moving along a circle in real space acquires a geometric phase.[1] In a lattice, if one chooses the parameter on which the Hamiltonian depends, to be the crystal momentum k, and moves a particle along a closed loop in momentum space, the particle acquires a geometric phase. In this case, the curl of Berry connection (the Berry curvature) essentially defines a 'magnetic field in the reciprocal space'. Another example is the position-dependent Hamiltonian

$$H(\vec{r}) = -\mu.B(\vec{r}), \tag{1.2}$$

of a neutral particle with magnetic moment μ moving in a plane perpendicular to a nonuniform magnetic field. The local eigenstates are calculated from the Schrödinger equation $H|\psi_m(\vec{r}(t))\rangle = E_m(\vec{r}(t))|\psi_m(\vec{r}(t))\rangle$. If the particle starts at $\vec{r}_0$ in a local eigenstate $|\psi_m(\vec{r}_0)\rangle$, and moves in the real space adiabatically under the nonuniform magnetic field, so that at all times it remains in the local eigenstate $|\psi_m(\vec{r}(t))\rangle$. At any time, the wave function acquires a dynamical phase factor of $e^{-\frac{i}{\hbar}\int_0^t \mathrm{d}\, t' E_m(\vec{r}(t))}$ due to the time evolution. When the particle returns to its initial position $\vec{r}_0$, its wave function is again given by the local eigenstate $|\psi_m(\vec{r}_0)\rangle$. But, aside from the time-evolution phase factor, let us also allow a phase factor that might result from the position dependency of the eigenstates,

$$e^{i\varphi_m}|\psi_m(\vec{r}_0)\rangle. \tag{1.3}$$

This geometrical phase factor can be easily calculated by inserting the wave function into the time-dependent Schrödinger equation $i\hbar\partial_t|\psi_m(t)\rangle = H(\vec{r}(t))|\psi_m(t)\rangle$ as [13]

$$\varphi_m = \oint \mathrm{d}\,\vec{r}\, i\langle\psi_m(\vec{r})|\partial_{\vec{r}}|\psi_m(\vec{r})\rangle. \tag{1.4}$$

In a cold atom setting, dressed states play the role of the adiabatic eigenstates. In the original experiment by Lin *et al.*, the NIST group used ^{87}Rb $F = 1$ hyperfine states [1]. They first applied a real magnetic field to Zeeman split

[1] Here, one must note that to simulate the cyclotron motion resulting from the Lorentz force $\vec{F} = \vec{v} \times q\vec{B}$, the crucial ingredient is to have nonvanishing $q\vec{B}$ product, not the magnetic field itself nor the charge. So, for a general coupling appearing in the Hamiltonian in the form of $(\vec{p} - \alpha\vec{r})^2$, one can always assign an effective charge q^* and an effective magnetic field B^*, for which the cyclotron frequency is given by $\omega = \sqrt{\hbar/q^*B^*}$.

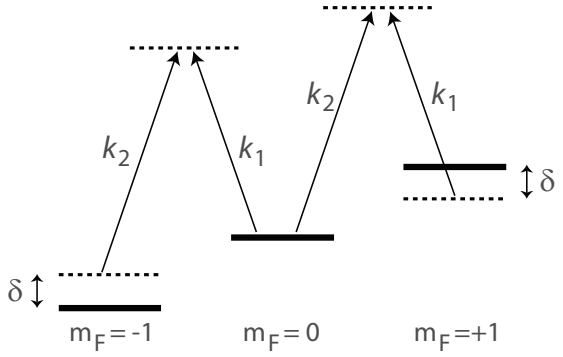

Figure 1.1: Illustration of the dressed states of a system in $F = 1$ hyperfine level, representing the experimental scheme employed by Ref. [1]. The sublevels are first split by a real magnetic field (dotted lines for $m_F = \pm$), and then coupled with resonant Raman transitions $k_{1,2}$. Then a second, position-dependent Zeeman shift is applied (solid lines), creating a spatially changing detuning $\delta(r)$. So, the energy of the dressed states will change with position, and a particle adiabatically following such a dressed state will experience a geometric phase.

the sublevels $m = 0, \pm 1$ and lift the degeneracy. Then, by using off-resonant Raman lasers, they dressed the atomic energy levels (see Fig. 1.1). The system is initially prepared in the eigenstate with the lowest eigenvalue of this atom-light coupling. The eigenenergies of these atomic dressed states can be made position dependent, by making the Raman coupling position dependent. This can be achieved, for example, by a spatially changing detuning of the laser frequency or a spatially changing laser intensity. The NIST group employed a position-dependent detuning; i.e. along one spatial direction, let us say $\hat{y}$, they uniformly changed the detuning δ between the atomic states and the Raman transitions, which can be easily achieved by implementing a position dependent Zeeman shift for these atomic levels. If the particles move slowly enough, they adiabatically follow the lowest energy dressed state at each y-point in space. Therefore, the position dependence of the eigenstates results in a geometric phase.

Raman-coupling of the internal degrees of freedom of the atoms has facilitated the realization of synthetic gauge fields in various setups, and even been used to create synthetic dimensions [14, 15]. However, all of these AMF experiments have employed only a single atomic species. In this thesis, we point out an important, yet hitherto unexplored, aspect of the AMFs. The techniques described

above inducing the geometric phases are highly sensitive to the internal degrees of freedom of the atoms. Therefore, if one applies this scheme to a mixture of two different atomic species, or to a mixture of the same species at different hyperfine levels, the resulting coupling will be different for the two components. For example, the g-factors for ^{87}Rb $5S_{1/2}$ $F = 1$ and ^{85}Rb $5S_{1/2}$ $F = 2$ have a $3/2$ ratio. If the original recipe implemented by Ref. [1] is to be applied to a mixture of these atoms at different hyperfine levels, position dependent detunings, consequently the AMFs, would reflect this ratio.

This unequal coupling to the different components of a system can have non-trivial consequences, testing the limits of orbital magnetism effects, or can be implemented as a probe for the response of the system. In the next chapter, we first consider a one-dimensional Fermi gas trapped in a ring geometry (the results are published in Phys. Rev. A 91, 053625 (2015)). We then drop an atom from another species or hyperfine level among the fermions, and consider an AMF coupling specifically to the impurity atom. When the impurity is interacting with the fermionic background, we can pump angular momentum to the fermions by using the AMF. We show that such an AMF is a versatile tool to investigate the impurity dynamics and the polaron formation. Using Bethe Ansatz, we calculate the eigenstates and corresponding energies exactly as a function of the flux passing through the toroidal trap. Adiabatic change of flux connects the ground state to excited states due to flux quantization. We consider contact interactions between the impurity and fermions, and analyze the full spectrum for the interaction strength, from the infinitely-strong attractive to the infinitely-strong repulsive limit. The impurity atom perturbs the Fermi sea by dragging the fermions whose momentum matches the flux, and this drag transfers momentum from the impurity to the background. Analyzing this angular momentum transfer can help us understand the angular momentum transfer occurring at larger scales between two different species in a mixture which are rotating at different rates. One must also analyze the effect of interactions on the effective mass of the impurity. For attractive interactions, formation of a dimer from the impurity and one fermion can be also investigated in detail by using the AMF.

In Chapter 3, we turn our attention to one of the most intriguing concepts of

condensed matter theory; superconductivity. In the semiclassical approximation, critical temperature of a superconductor decreases with applied magnetic field. However, if one includes the Landau level (LL) structure at high field values, the critical temperature surprisingly starts increasing with some oscillations (see Fig. 3.1). This high-field superconductivity was first predicted by Tešanović in 1989 [16]. However, an experimental observation has been elusive due to the high magnetic field values required in a solid state system to confine particles into their first few LLs, not even mentioning the low temperatures required to observe the quantization effects. In Chapter 3, we propose to use light-induced AMFs in cold atoms to investigate the superconducting phase diagram in the strong coupling limit (the results are published in Phys. Rev. Lett. 116, 045305 (2016)). In the cold atom context, two different atomic species or two different hyperfine states would play the role of up and down spins forming the Cooper pairs, and therefore, resulting in an unequal coupling to the AMF. This enables the study of Bardeen-Cooper-Schrieffer (BCS) pairing of fermions with unequal effective charges. This constitutes a fundamental extension of the BCS theory, in addition to the studies on pairing in the presence of density [17, 18] or mass imbalance [19, 20]. We investigate the superconducting phase diagram of a system formed by such pairs of unequal effective charges as a function of field strength. We consider a homogeneous two-component Fermi gas of unequal effective charges with attractive contact interactions. We employ a two-channel model to describe the system and analytically calculate the Gap equation at the transition point.

Finally, aside from mixtures, one can also simulate various condensed matter models by using synthetic gauge fields in the clean environment of cold atoms; such as the topologically protected states which have attracted great interest of the condensed matter community over the last decades. Thouless, Kosterlitz and Haldane were awarded the Nobel Prize in Physics in 2016 for their contribution to the theory of topological phases of matter [21]. The Haldane model is a simple yet realistic topological lattice model which realizes quantum Hall effect in the absence of an external magnetic field [22]. Since its proposal in 1988, the Haldane model has been constantly studied by theorists to investigate topologically protected states of matter. However, its experimental observation has only

been achieved in a cold atom setting [23], by implementing an AMF in an optical lattice. Recent cold-atom realizations [23, 24, 25, 26, 27, 28] open up the possibility of exploring topological response in different limits enabled by the high controllability of the experiments.

Depending on the staggered magnetic field passing through a unit cell, the Haldane model can be either in a topologically trivial state or have ± 1 Chern number. Therefore, by suddenly quenching the magnetic field value, one can drive the system across a topological phase boundary. This is something impossible to implement in a solid state setting, because a sudden change of a real magnetic field would induce Eddy currents and inevitably heat the system. In cold atoms, however, magnetic fields are created artificially and one can study quenches between Hamiltonians with different magnetic field values. In Chapter 4, we theoretically investigate the Hall response of a lattice system following a quench where the topology of a filled band is suddenly changed (the results are published in Phys. Rev. A 94, 053604 (2016)). Aspects of the original topology survive the quench, but most physical observables (edge currents, Hall conductivity) appear to be non-universal. In the limit where the physics is dominated by a single Dirac cone, we find that the change in the Hall conductivity is two-thirds of the quantum of conductivity. We explore this universal behavior in the Haldane model, and discuss cold-atom experiments for its observation.

Chapter 2

Impurity under an Artificial Magnetic Field

The dynamics of a single impurity interacting with a many-particle background is one of the central problems of condensed-matter physics. Several condensed-matter models can be reduced to a problem of an impurity interacting with a reservoir. Depending on the type of the impurity (magnetic/nonmagnetic, stationary/mobile, charged/neutral ...), the type of the interactions in the system (contact, dipolar ...), or the specifics of the system (fermionic, bosonic, dimensionality ...), a wide range of phenomena can be observed in this setup [29, 30, 31, 32, 33, 34, 35]. Compared to a full-scale many-body problem, the dynamics of an impurity is generally easier to treat where the most interesting physics emerges around the impurity and, hence, can be controlled in a better way. This, however, does not imply that it is trivial. The collective behavior of the system can be quite unconventional as in the Kondo effect [29] or the polaron formation [31, 35]. Therefore, it is fundamentally important to examine how these novel phenomena emerge from the underlying interactions between the building blocks of the system.

Here, we consider an impurity atom in a cold atom setting. If one creates an artificial magnetic field (AMF) in the system by coupling light to the internal

states of the atoms, the effect will be highly sensitive to the internal degrees of freedom of the particles. So, the resulting effective magnetic field acting on the impurity atom and the background atoms will be different. We argue that an AMF coupling specifically to the impurity is an efficient way to probe the polaron state.

For the theoretical study of an impurity, one generally resorts to some form of approximation, e.g. by averaging out the effect of the background. An exact solution for a many-body system is rare in the literature. One great example for such an exact solution is the Bethe Ansatz (BA) in one dimension. The BA solution has been generalized to many integrable models, e.g. systems with multiple components, different statistics or spin [36, 37, 38, 39, 40]. This exact solution method has been employed to explain experimental data on a number of instances [41, 42]. However, as BA methods are restricted to one dimension, they have not been used to describe systems where an external artificial gauge field is present.

In one dimension, such an external magnetic field can be disregarded by using a gauge transformation, unless the one dimensional system closes onto itself. Thus, if the particles are confined to a ring as opposed to a line segment, the AMF will significantly effect the physics. Such rings, in the form of toroidal traps, have been realized experimentally [43, 44, 45, 46, 47, 48, 49, 50], although none of these experiments have included an artificial gauge field so far. When the radial extent of a toroidal trap is small, so that only a single mode is supported in the radial direction, the system becomes quasi one dimensional and can be treated exactly with BA.

Here, we consider a one-dimensional spin polarized Fermi gas trapped in a ring geometry and drop an impurity atom among them (see Fig. 2.1 for the illustration). In the cold-atom context, both the impurity and the fermions are neutral atoms. Under an AMF coupling exclusively to the impurity, it will act like a charged particle among the uncharged fermions. We imagine an AMF along the axis of ring by the use of which we can pump angular momentum to the system. The charged impurity is expected to drag the uncharged fermions along

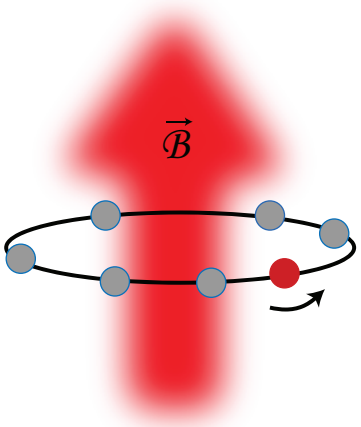

Figure 2.1: A simple illustration of the system. $N-1$ uncharged fermions (light gray) and a single charged impurity (dark gray) are trapped on a ring. The impurity is interacting with the fermions via Delta-function interaction. An AMF couples exclusively to the impurity. The dynamics of the system depends on the interaction strength between particles and the total flux through the ring $\beta = \frac{qRA}{\hbar}$. ©2015 APS

with itself around the ring. Because of the interactions between the impurity and the background atoms, a collective excitation usually called a polaron, is formed [51]. This excitation will couple to the external magnetic field with the charge of the impurity particle, however, its mass will critically depend on the interaction strength. The amount of angular momentum carried by the impurity and the uncharged fermions also depend on the total external flux through the ring. By changing the AMF strength, it is possible to access excited states of the system adiabatically. We describe this system exactly using a BA solution for contact interactions, which are justified for cold atoms since the dominant scattering is s-wave, and show that using an AMF coupling the impurity would be a very effective tool to observe the resulting polaron physics.

This chapter is organized as follows: In the next section, we define the model, introduce the notation and review earlier studies. In Section 2.2.1, we solve the system for two particles and then generalize to any particle number using the BA in Sec. 2.2.2. Sec. 2.3 presents the analytical solution of the BA equations in certain limits and the comparison with numerical solutions. We calculate several

quantities such as energy, angular momentum and effective mass of the charged particle.

The discussion presented in this chapter is based on the material published in Ref. [52].

2.1 The Model

The Schrödinger equation for one charged particle under a magnetic field among $N-1$ uncharged fermions of equal mass m reads

$$H\Psi = E\Psi,$$

$$\frac{1}{2m}\Big(\frac{\hbar}{i}\frac{\partial}{\partial x_1} - qA\Big)^2 - \frac{\hbar^2}{2m}\sum_{j=2}^{N}\frac{\partial^2}{\partial x_j^2} + 2c\sum_{j=2}^{N}\delta(x_1 - x_j)\Psi(x_1, x_2..x_N) = E\Psi(x_1, x_2..x_N), \tag{2.1}$$

in the first quantized form. All particles are assumed to be on a ring of radius R; $0 \leq x_i \leq 2\pi R$. The position of the charged particle is x_1 and A is the vector potential in the symmetric gauge. The impurity interacts with the background atoms with contact interactions of strength c. The Hamiltonian can be adimensionalized by using the radius of the ring: $\tilde{x}_j = \frac{x_j}{R}$, $\tilde{E} = E\frac{2mR^2}{\hbar^2}$, $\tilde{c} = c\frac{2mR}{\hbar^2}$ and $\beta = \frac{qRA}{\hbar}$, where β is the total magnetic flux through the ring in units of flux quantum q/h. We then drop the tildes for simplicity, so that the Hamiltonian is given by

$$\mathcal{H} = \Big(-i\frac{\partial}{\partial x_1} - \beta\Big)^2 - \sum_{j=2}^{N}\frac{\partial^2}{\partial x_j^2} + 2c\sum_{j=2}^{N}\delta(x_1 - x_j). \tag{2.2}$$

The effect of the magnetic field can be shifted to the boundary conditions ($\Psi(x_1 + 2\pi, x_2..x_N) = \Psi(x_1, x_2..x_N)$) by a gauge transformation [53],

$$\underbrace{e^{-i\beta x_1}He^{i\beta x_1}}_{H'}e^{-i\beta x_1}\Psi(x_1, x_2..x_N) = Ee^{-i\beta x_1}\Psi(x_1, x_2..x_N) \tag{2.3}$$

$$\overbrace{\Big[-\sum_{j=1}^{N}\partial_j^2 + 2c\sum_{j=2}^{N}\delta(x_1 - x_j)\Big]}\Psi'(x_1, x_2..x_N) = E\Psi'(x_1, x_2..x_N), \tag{2.4}$$

where $\Psi' = e^{-i\beta x_1}\Psi$, and we again drop the prime-sign on Ψ in the following. Namely, when the first particle (charged impurity) makes a full circle around the ring the wave function gains a phase factor of $e^{i\beta 2\pi}$ where the periodic boundary conditions (PBCs) for the uncharged particles remain unaffected by the gauging process.

Apart from the twisted boundary conditions (BCs), the δ-function interaction serves as two-sided BC between two different regions of space which are essentially different permutations of particles. This discontinuity relation can be obtained easily by passing to the center of mass (z) and relative coordinates (y),

$$\left.\begin{array}{l} y = x_1 - x_2 \\ z = \frac{x_1+x_2}{2} \end{array}\right\} \quad \left.\begin{array}{l} \partial_1 = \partial_y + \frac{1}{2}\partial_z \\ \partial_2 = -\partial_y 1 + \frac{1}{2}\partial_z \end{array}\right\} \quad \begin{array}{l} \partial_y = \frac{1}{2}\partial_1 - \frac{1}{2}\partial_2 \\ \partial_z = \partial_1 + \partial_2. \end{array} \tag{2.5}$$

By integrating the Hamiltonian with respect to the relative coordinate for $\int_{-\epsilon}^{+\epsilon} \mathrm{d}y$ when $\epsilon \to 0$,

$$\int_{0^-}^{0^+} \mathrm{d}y \quad \to \quad \left[-2\partial_y^2 - \frac{1}{2}\partial_z^2 + 2c\delta(y) \right] \Psi(y,z) = E\Psi(y,z), \tag{2.6}$$

we obtain the two-sided discontinuity relation for contact interactions,

$$2\partial_y \Psi(y,z)\Big|_{0^-}^{0^+} = 2c\delta(y)\Psi(y=0,z). \tag{2.7}$$

By going back to normal coordinates, we find the discontinuity relation at the boundary $x_1 = x_j$ as

$$(\partial_j - \partial_1)\psi\Big|_{x_1<x_j} - (\partial_j - \partial_1)\psi\Big|_{x_j<x_1} = 2c\psi\Big|_{x_j=x_1}, \quad j \neq 1. \tag{2.8}$$

This one-dimensional problem of two-component fermions has been studied by using the BA in the previous century. First, the one-spin deviate problem in a Fermi sea is solved by McGuire [39], then Flicker and Lieb [54] solved the two-spin deviate problem. Yang [38] elegantly derived the BA equations for the general M down-spins among N up-spins. Twisted BCs have been used throughout the BA literature as a way to probe ground state properties. However, with the possibility of optically inducing AMFs, it is important to calculate the properties

of the system at finite flux as opposed to infinitesimal values near zero. It is also necessary to consider cases where different components in the system experience different gauge fields.

Our calculation takes both of these constraints into account and allows us to exactly study the dynamics resulting from the dragging effect of the charged particle on the uncharged particles. The resulting polaron physics has attracted great interest in the context of cold atoms over the last few years [51, 55].

2.2 The Ansatz

As the interactions are reduced to BCs, the wave function for a given permutation of the particles can be written as a superposition of plane waves. Since the collisions of equal mass particles in one dimension conserve magnitudes of the incoming momenta, the interacting problem is integrable. Hence, in a given region only a finite number of plane waves are needed to construct the wave function. To make our notation clear, we first start with the case of one charged particle with one neutral particle.

2.2.1 $N = 2$ Particles

For two particles we have $2! = 2$ regions and the wave function in these regions is expressed as follows:

$$R_1 : x_1 < x_2 \qquad \Psi_{12}(x_1, x_2) = (12)_{12} e^{i(k_1 x_1 + k_2 x_2)} + (21)_{12} e^{i(k_2 x_1 + k_1 x_2)} \tag{2.9}$$

$$R_2 : x_2 < x_1 \qquad \Psi_{21}(x_1, x_2) = (12)_{21} e^{i(k_1 x_1 + k_2 x_2)} + (21)_{21} e^{i(k_2 x_1 + k_1 x_2)} \tag{2.10}$$

where we use parenthesis with a subscript to indicate the coefficients of plane waves. In this notation numbers in the parenthesis indicate the order the wave vectors k_1, k_2 are distributed to the coordinates in the exponent and the subscript indices indicate the ordering of the particles on the ring, *i.e.* Ψ_{12} means $x_1 < x_2$. At $x_1 = x_2$, the wave functions in these two regions should be equal whereas their

derivative should obey Eq.2.8. Equating the coefficients of each plane wave on both sides, we obtain:

BCs: at $x_1 = x_2$,

$$(12)_{21} + (21)_{21} = (12)_{12} + (21)_{12}, \tag{2.11}$$

$$(12)_{21} - (21)_{21} = (12)_{12}\Big(1 + \frac{2}{s_{12}}\Big) + (21)_{12}\Big(-1 + \frac{2}{s_{12}}\Big), \tag{2.12}$$

where $s_{12} = i(k_1 - k_2)/c$. Combined BCs (continuity of the wave function and discontinuity of its derivative) give

$$\begin{pmatrix} (12) \\ \\ (21) \end{pmatrix}_{21} = \begin{pmatrix} 1 + \frac{1}{s_{12}} & \frac{1}{s_{12}} \\ \\ \frac{-1}{s_{12}} & 1 - \frac{1}{s_{12}} \end{pmatrix} \begin{pmatrix} (12) \\ \\ (21) \end{pmatrix}_{12}. \tag{2.13}$$

Allowed values for k_1, k_2 are found by applying the PBCs. PBC for one of the particles gives the BA equation.

Twisted BCs: at 2π

as $x_2 : 0 \to 2\pi$, $\quad \Psi_{21}(x_2 = 0) = \Psi_{12}(x_2 = 2\pi)$,

$$(12)_{21} = (12)_{12} e^{ik_2 2\pi}, \qquad (21)_{21} = (21)_{12} e^{ik_1 2\pi}. \tag{2.14}$$

as $x_1 : 0 \to 2\pi$, $\quad \Psi_{12}(x_1 = 0) = e^{i\beta 2\pi}\Psi_{21}(x_1 = 2\pi)$,

$$(12)_{12} = (12)_{21} e^{i(k_1+\beta)2\pi}, \quad (21)_{12} = (21)_{21} e^{i(k_2+\beta)2\pi}. \tag{2.15}$$

Combining the two BCs at 2π, we obtain another constraint $k_1 + k_2 + \beta = n$, for $n \in \mathbb{Z}$. This is a reflection of the total angular momentum conservation in the system. Eqs.2.13 and Eq.2.15 have non-trivial solutions only when the determinant below vanishes,

$$\begin{pmatrix} (12) \\ \\ (21) \end{pmatrix}_{21} = \begin{pmatrix} 1 + \frac{1}{s_{12}} & \frac{1}{s_{12}} \\ \\ \frac{-1}{s_{12}} & 1 - \frac{1}{s_{12}} \end{pmatrix} \begin{pmatrix} (12) \\ \\ (21) \end{pmatrix}_{12} = \begin{pmatrix} e^{-i(k_1+\beta)2\pi}(12)_{12} \\ \\ e^{-i(k_2+\beta)2\pi}(21)_{12} \end{pmatrix} \tag{2.16}$$

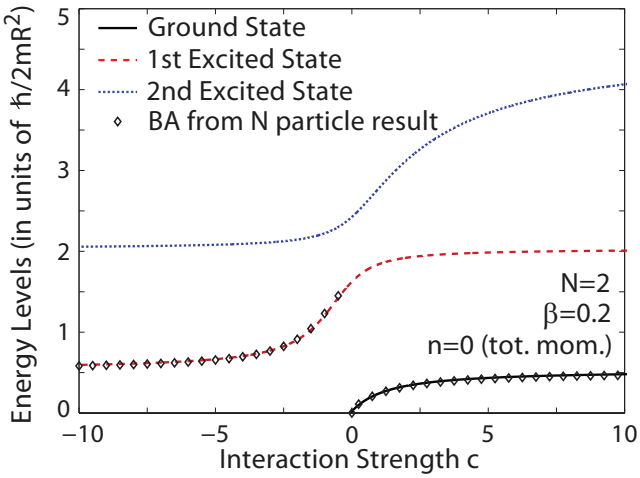

Figure 2.2: Energy of the three lowest states vs. interaction strength for $N = 2$ particles, and zero total angular momentum. Only scattering states are displayed. Energy is calculated in three different ways. Lines are from Eq.2.19 direct analytical solution without employing BA, which is algebraically same as the two-particle BA calculation (Eq.2.18). Diamonds are from the general N-particle BA calculation (Eq.2.27). ©2015 APS

$$\begin{vmatrix} 1+\frac{1}{s_{12}}-e^{-i(k_1+\beta)2\pi} & \frac{1}{s_{12}} \\ \frac{-1}{s_{12}} & 1-\frac{1}{s_{12}}-e^{-i(k_2+\beta)2\pi} \end{vmatrix} = 0. \tag{2.17}$$

The solution of this determinant gives the BA equation,

$$\alpha = \frac{c}{2}\cot\left(\frac{\pi}{2}(\alpha+n-\beta)\right)+\frac{c}{2}\cot\left(\frac{\pi}{2}(\alpha-n+\beta)\right), \tag{2.18}$$

where energy is $E = \frac{(n-\beta)^2+\alpha^2}{2}$ for $\alpha = k_2 - k_1$. For the two-particle case, this problem can also be solved exactly without using the BA [56],

$$c = \alpha\left(\frac{\cos(\pi(n-\beta))}{\sin(\pi\alpha)}-\cot(\pi\alpha)\right). \tag{2.19}$$

These two equations (Eqs. (2.18) and (2.19)) analytically reproduce each other and the numerical results match perfectly (Fig.2.2).

Extension of this method to N particles is straightforward if cumbersome.

2.2.2 $N-1$ Fermions, One Charged Particle

The distinguishable charged particle is denoted again by x_1 and the wave function is defined in $N!$ regions corresponding to different permutations [39]. In each one of these regions, the wave function consists of $N!$ plane waves in its most general form without imposing the antisymmetry between the fermions. As a total, we have $N! \times N!$ coefficients:

$$\begin{aligned}
\Psi_{123\ldots} &= (123\ldots)_{123\ldots} e^{i(k_1x_1+k_2x_2+k_3x_3+\ldots)} + (213\ldots)_{123\ldots} e^{i(k_2x_1+k_1x_2+k_3x_3+\ldots)} + \ldots \\
\Psi_{213\ldots} &= (123\ldots)_{213\ldots} e^{i(k_1x_1+k_2x_2+k_3x_3+\ldots)} + (213\ldots)_{213\ldots} e^{i(k_2x_1+k_1x_2+k_3x_3+\ldots)} + \ldots \\
\Psi_{132\ldots} &= (123\ldots)_{132\ldots} e^{i(k_1x_1+k_2x_2+k_3x_3+\ldots)} + (213\ldots)_{132\ldots} e^{i(k_2x_1+k_1x_2+k_3x_3+\ldots)} + \ldots \\
&\vdots \qquad\qquad\qquad\qquad \vdots
\end{aligned} \tag{2.20}$$

where $k_1, k_2, \ldots k_N$ are distinct wavenumbers. BCs at $x_1 = x_2$ are not effected by the addition of other fermions at the end of the sequence:

$$\begin{pmatrix} (123\ldots) \\ \\ (213\ldots) \end{pmatrix}_{213\ldots} = \begin{pmatrix} 1+\frac{1}{s_{12}} & \frac{1}{s_{12}} \\ \\ \frac{-1}{s_{12}} & 1-\frac{1}{s_{12}} \end{pmatrix} \begin{pmatrix} (123\ldots) \\ \\ (213\ldots) \end{pmatrix}_{123\ldots} . \tag{2.21}$$

BCs at 2π follow the same logic; as $x_2 : 0 \to 2\pi$

$$\begin{aligned}
\Psi_{213\ldots N}(x_2 = 0) &= \Psi_{13\ldots N2}(x_2 = 2\pi), \\
(123\ldots)_{213\ldots N} &= (123\ldots)_{13\ldots N2} e^{ik_2 2\pi}, \\
(213\ldots)_{213\ldots N} &= (213\ldots)_{13\ldots N2} e^{ik_1 2\pi}.
\end{aligned} \tag{2.22}$$

Number of independent coefficients decreases considerably by requiring antisymmetry upon exchange of fermions. Every coefficient of a plane wave in region $x_1 < x_3 < x_2 < \ldots < x_N$ is identical with the coefficient of the same plane wave in region $x_1 < x_2 < x_3 < \ldots < x_N$, i.e. $(\textit{some permutation})_{132} = (\textit{the same permutation})_{123}$. This can be shown by noticing that at $x_2 = x_3$ the wave function in a given region must vanish, requiring *e.g.* $(123\ldots)_{123\ldots N} =$

$-(132\ldots)_{123\ldots N}$. Fermionic antisymmetry also relates the wave functions in separate regions; $\Psi_{123\ldots N} = -\Psi_{132\ldots N}$. As a result, the coefficients only depend on the position of the charged particle in the order. We can move indistinguishable fermions through one another at will and the $N!$ regions reduce to N regions.

After this simplification it is easy to combine the BC at a δ-function with the overall PBC.

$$\begin{aligned}\begin{pmatrix}(123\ldots)\\ \\ (213\ldots)\end{pmatrix}_{213\ldots N} &= \begin{pmatrix}1+\frac{1}{s_{12}} & \frac{1}{s_{12}}\\ \\ \frac{-1}{s_{12}} & 1-\frac{1}{s_{12}}\end{pmatrix}\begin{pmatrix}(123\ldots)\\ \\ (213\ldots)\end{pmatrix}_{123\ldots N}\\ &= \begin{pmatrix}e^{ik_2 2\pi}(123\ldots)_{123\ldots N}\\ \\ e^{ik_1 2\pi}(213\ldots)_{123\ldots N}\end{pmatrix}. \end{aligned} \tag{2.23}$$

The determinant can only vanish if k_1 and k_2 satisfy,

$$k_1 - \frac{c}{2}\cot \pi k_1 = k_2 - \frac{c}{2}\cot \pi k_2. \tag{2.24}$$

Remember that these conditions are obtained by using the BCs at $x_1 = x_2$ and by using the first two pairs of plane waves in the wave functions (the coefficients in front of the $e^{ix_1(k_1+k_2)+ik_3x_3}$ term). However, there are other plane waves in this same BC, e.g. $((231)_{123} + (321)_{123})e^{ix_1(k_2+k_3)+ik_1x_3}$ term. If we write down the BCs for these terms, we will obtain relations between other momenta (e.g. between k_2 and k_3 for the given plane wave). Alternatively, we can obtain the relations between other momenta by writing the BCs between other particles, for example BCs at $x_1 = x_3$. These two approaches produce the same result, and all the wavenumbers must satisfy

$$k_1 - \frac{c}{2}\cot \pi k_1 = k_2 - \frac{c}{2}\cot \pi k_2 = k_3 - \frac{c}{2}\cot \pi k_3 = \ldots = \lambda,$$

where λ is a real constant. This form is equivalent to the usual BA equations [37].

Hence, the N wavenumbers which define an eigenstate must be chosen as N distinct roots of the equation:

$$k - \lambda = \frac{c}{2}\cot \pi k. \tag{2.25}$$

However, there is another constraint. Applying PBCs sequentially on all particles restricts λ.

$$\text{As } x_1 : 0 \to 2\pi, \qquad \Psi_{123\ldots N}(x_1 = 0) = e^{i\beta 2\pi}\Psi_{23\ldots N1}(x_1 = 2\pi),$$

$$(123)_{123} = (123)_{231}e^{i(\beta+k_1)2\pi},$$

$$\begin{aligned} \text{as } x_2 : 0 \to 2\pi, \qquad & (123)_{231} = (123)_{312}e^{ik_2 2\pi}, \\ \text{as } x_3 : 0 \to 2\pi, \qquad & (123)_{312} = (123)_{123}e^{ik_3 2\pi}, \\ \vdots \qquad & \vdots \end{aligned}$$

In combination:

$$(123\ldots)_{123\ldots N} = e^{i(k_1+k_2+\ldots+k_N+\beta)2\pi}(123\ldots N)_{123\ldots N}, \tag{2.26}$$

reflecting angular momentum conservation: Sum of all the wavenumbers plus the flux must be integer on a ring.

In short, the BA equation is solved by finding N roots of a simple equation (see Fig. 2.3) subject to the angular momentum constraint:

$$k - \lambda = \frac{c}{2}\cot \pi k, \qquad \sum_j^N k_j = n - \beta, \quad n \in \mathbb{Z}. \tag{2.27}$$

So far our treatment implicitly assumed repulsive interactions. In which case, all the wavevectors k_i are real. The ansatz can easily be extended to attractive interactions yielding exactly the same equations Eq.2.27 [57]. However, for negative c two of the roots will be complex, as the δ-potential in one dimension has only a single bound state.

2.3 Solution of the BA Equation

The $\cot \pi k$ term in Eq.2.27 diverges at every integer k, thus, regardless of the value of β (or λ) there is a root between every consecutive integer (Fig.2.3). By changing the value of λ, all roots can be adjusted so that the total angular

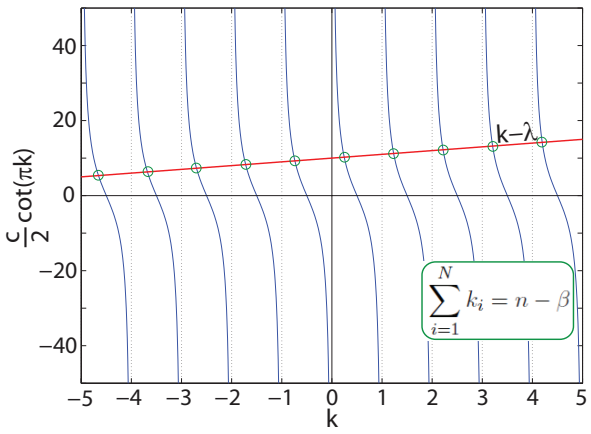

Figure 2.3: A representation of graphical solution to BA equation. The $\cot \pi k$ term in Eq.2.27 diverges at every integer k and there is a root between every consecutive integer independently from $\lambda(\beta)$. By changing the value of λ, all roots can be adjusted so that the total angular momentum constraint is satisfied. ©2015 APS

momentum constraint is satisfied. All the eigenstates in this problem can be labeled identically by choosing N distinct integers corresponding to the different branches of $\cot \pi k$ and the total angular momentum $n \in \mathbb{Z}$. The energy of an eigenstate is simply the sum of squares of all wavenumbers

$$E = \sum_{i=1}^{N} k_i^2. \tag{2.28}$$

For the simplest case of $\beta = 0$, the ground state corresponds to $\lambda = 0$ and the total angular momentum $n = 0$. The roots k are distributed symmetrically around zero for even N, hence, automatically satisfy the total angular momentum condition. The wavevectors for the ground state are in the N branches of *cot* from $-N/2$ to $N/2$. Excitations above this ground state can be generated by two procedures. First, by changing λ, N roots which are on the same branches of *cot* can be generated so as to create an eigenfunction with non-zero total angular momentum ($n \neq 0$). Second, at least one of the roots can be chosen to reside on a branch that is not occupied for the ground state. For such a particle-hole excitation, λ must be adjusted to ensure the total angular momentum constraint.

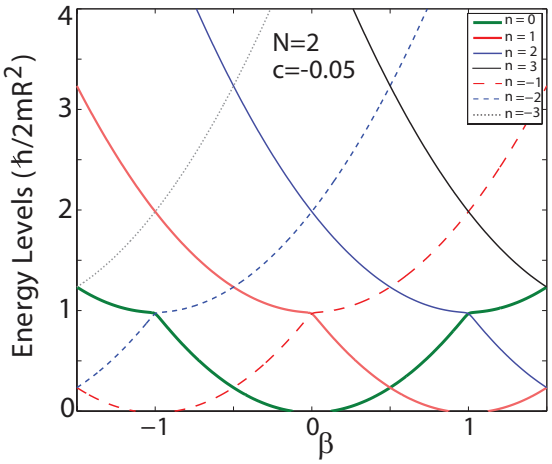

Figure 2.4: Ground state energy vs. flux β for $N = 2$ particles with total angular momentum n. Eigenstates for flux β with total angular momentum n are also eigenstates for flux $\beta + 1$ with total angular momentum $n + 1$. The system can be analyzed by considering flux values between $-1/2 < \beta < 1/2$ for all n. As the flux is increased by one adiabatically, the system evolves to a higher excited state which has one more unit of total angular momentum. The crossings between different eigenstates is not a problem for adiabatic evolution since only states with different total angular momentum n are degenerate. ©2015 APS

Inclusion of the magnetic field affects only the total angular momentum constraint. As that constraint is defined only up to an integer (n), the problems with values of β differing by an integer are identical. Eigenstates for flux β which have total angular momentum n are also eigenstates for flux $\beta + 1$ which have total angular momentum $n + 1$. This is a restatement of flux quantization. We can analyze the system by considering flux values between $-1/2 < \beta < 1/2$.

However, in an experimental setting slowly increasing the value of the flux through the ring is a useful method to access excited states. As the flux is increased adiabatically from zero to one, the ground state evolves to an eigenstate which has its roots exactly in the same branches as the ground state, but, has a total angular momentum of minus one at zero flux (Fig.2.4). The crossings between different eigenstates do not pose a problem for adiabatic evolution as only states with different total angular momentum n can be degenerate in energy.

The BA equation Eq.2.27 can be very efficiently solved once the regions for the roots are determined. We used the Newton-Raphson algorithm to find a solution

within a particular region. As all the roots depend monotonically on λ, another Newton-Raphson search is employed to satisfy the total angular momentum condition. We have found numerical solutions for systems of up to 10000 particles with high accuracy.

Although numerically solving the BA equation is efficient and accurate, an analytic solution can provide more insight about the physics of the system. Analytic formulae for energy, angular momentum and effective mass also would be desirable to make correspondence with experimental observations.

In the limit of strong interactions $1/c \ll 1$ and large particle number $N/c \gg 1$, such an analytic form can be obtained by approximating the roots of the BA equation. In this limit, because the *cot* diverges quickly near integers, most of the roots are close to integers. Apart from the few roots near $k \sim \lambda$, if we say that the s-th positive root occur at $k_s = s + \Delta$ where Δ is small, the BA equation follows

$$\frac{2}{c}(s + \Delta - \lambda) = \cot(s\pi + \Delta\pi) \qquad \Longrightarrow \quad \Delta \approx \frac{1}{\pi}\cot^{-1}\frac{2}{c}(s - \lambda), \tag{2.29}$$

where Δ/c term is extremely small and omitted. So, we find that the roots occur at

$$\begin{aligned} k_s^+ &= s + \frac{1}{\pi}\mathrm{acot}\frac{2}{c}(s - \lambda), \\ k_s^- &= -s - \frac{1}{\pi}\mathrm{acot}\frac{2}{c}(s + \lambda), \quad s = 0, 1, \ldots, \frac{N}{2} - 1, \end{aligned} \tag{2.30}$$

where *acot* is defined in the continuous region $(0, \pi)$ for Eqs.2.30 to be accurate guesses. Here we have restricted s to analyze the ground state and excited states with roots on the same *cot* branches. Applying the total angular momentum

condition we get,

$$\begin{aligned} n-\beta &= \sum_{s=0}^{N/2-1} k_s \\ &= \frac{1}{\pi}\sum_{s}^{N/2-1}\Big(\mathrm{acot}\frac{2}{c}(s-\lambda)-\mathrm{acot}\frac{2}{c}(s+\lambda)\Big) \\ &= \frac{c}{2\pi}\int_0^{x_F}\mathrm{d}x\Big(\mathrm{acot}(x-b)-\mathrm{acot}(x+b)\Big) \\ &= \frac{-c}{2\pi}\int_{x_F-b}^{x_F+b}\mathrm{d}x\mathrm{acot}x+\frac{cb}{2}, \end{aligned} \tag{2.31}$$

with $b = 2\lambda/c$ and $x_F = k_F/c = (N-1/2)/c$. Here the initial assumption of strong interactions and large particle numbers allow us to approximate the sum by an integral. For the ground state and the first few excited states $n-\beta$ is small compared to N and the integral can be approximated by using $N/c \gg 1$ as

$$n-\beta = \frac{c}{2\pi}\int_{x_F-b}^{x_F+b}\mathrm{d}x\ \mathrm{atan}x \approx \frac{cb}{\pi}\mathrm{atan}x_F. \tag{2.32}$$

Through this relation b, hence λ, is obtained for any flux value, allowing us to find expressions for all the roots in a self consistent way.

2.3.1 Energy

Using these expressions for the roots, the total energy can be calculated as

$$\begin{aligned} E &= \sum_{s=0}^{N/2-1} k_s^2 \\ &= \sum_{s}^{N/2-1}\Big\{2s^2+\frac{2s}{\pi}\Big(\mathrm{acot}\frac{2}{c}(s-\lambda)+\mathrm{acot}\frac{2}{c}(s+\lambda)\Big) \\ &\qquad +\frac{1}{\pi^2}\Big((\mathrm{acot}\frac{2}{c}(s-\lambda))^2+(\mathrm{acot}\frac{2}{c}(s+\lambda))^2\Big)\Big\}. \end{aligned} \tag{2.33}$$

The first term above is the total ground state energy of $N-1$ non-interacting fermions. Interactions result in the second and third terms which are first and second order corrections in our expansion. When Δ's are small, the third term is

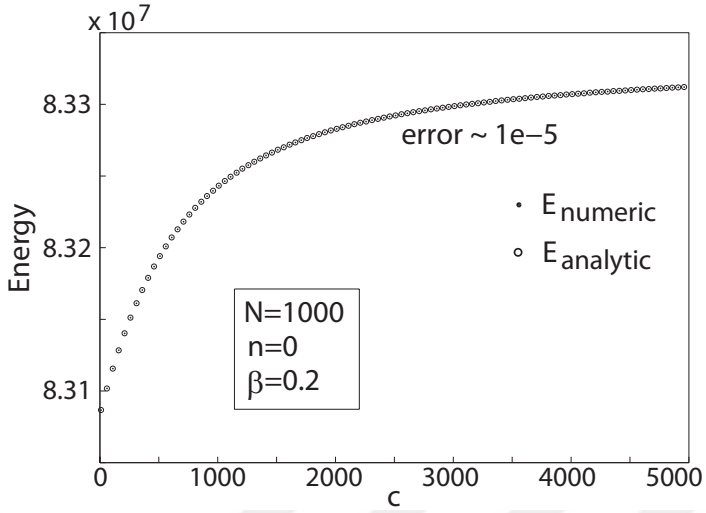

Figure 2.5: Ground state energy vs. interaction strength for $N = 1000$ particles and zero total angular momentum. Numerical solution of BA equation Eq.2.27 (dots) are virtually indistinguishable from analytical solution (circles) $E =$(Fermi energy of $N-1$ fermions)$+\Delta E$. Error between the numerical and analytical solutions are too small to observe even in the regimes where the assumptions for analytical calculation fails. ©2015 APS

negligible. In this limit, the energy shift due to repulsive interactions ($c > 0$) is:

$$\begin{aligned}
\Delta E &= \frac{c^2}{2\pi}\int_0^{x_F} \mathrm{d}x\, x\Big(\mathrm{acot}(x-b)+\mathrm{acot}(x+b)\Big) \\
&= \frac{c^2}{2\pi}\Bigg\{\int_{-b}^{x_F-b}\mathrm{d}x\, x\,\mathrm{acot}\,x \\
&\qquad +\int_b^{x_F+b}\mathrm{d}x\, x\,\mathrm{acot}\,x + b\Big(\underbrace{\int_{-b}^{x_F-b}\mathrm{d}x\,\mathrm{acot}\,x-\int_b^{x_F+b}\mathrm{d}x\,\mathrm{acot}\,x}_{\frac{2\pi}{c}(n-\beta)}\Big)\Bigg\} \\
&= cb(n-\beta)+\frac{c^2x_F^2}{4}-\frac{c^2}{2\pi}\int_{b-x_F}^{b+x_F}\mathrm{d}x\, x\mathrm{atan}\,x \\
&= cb(n-\beta)+\frac{c^2x_F^2}{4}-\frac{c^2}{4\pi}\Bigg\{\Big((x_F+b)^2+1\Big)\mathrm{atan}(x_F+b) \\
&\qquad +\Big((x_F-b)^2+1\Big)\mathrm{atan}(x_F-b)-2x_F\Bigg\} \qquad (2.34)
\end{aligned}$$

$$\text{with}\;\; b=\frac{\pi(n-\beta)}{c\;\mathrm{atan}(x_F)}.$$

This approximate form for energy successfully reproduces numeric results for particle numbers as small as 4 throughout all the interaction range. Ground state energy as a function of interaction strength is plotted for a typical case in Fig.2.5 for 1000 particles at $\beta = 0.2$ flux. The deviation between numerical and analytical results are too small to observe in this plot.

For attractive interactions, the δ-function interaction supports one bound state in one dimension. Corresponding imaginary wavevectors appear as solutions of the BA equation. For $k = \alpha + i\sigma$ with $(\alpha, \sigma) \in \mathbb{R}$, the BA equation has only two roots with $\sigma \neq 0$. The charged particle is bound with only one of the background fermions. When $1/|c| \ll 1$, the complex roots are at $k = \lambda \pm ic/2$ while the rest of the roots preserve their form given in Eqs.2.30. Within these approximations, we analytically calculate the total energy for attractive interactions,

$$\begin{aligned}\Delta E = & -\frac{c^2(b^2+1)}{2} + cb(n-\beta) + \frac{c^2 x_F^2}{4} \\ & + \frac{c^2}{4\pi}\left\{\Big((x_F+b)^2+1\Big)\mathrm{atan}(x_F+b) + \Big((x_F-b)^2+1\Big)\mathrm{atan}(x_F-b) - 2x_F\right\},\end{aligned} \tag{2.35}$$

$$\text{with } \; b = \frac{(n-\beta)}{c\Big(1 - \frac{1}{\pi}\mathrm{atan}(x_F)\Big)}.$$

If the bound state is narrow, Pauli repulsion between the fermion in the bound pair and background fermions decreases the effective interaction.

2.3.2 Angular Momentum

To understand the physics of the polaron formation and make correspondence to possible experiments, it is important to calculate other measurable quantities. In particular, for this system we are interested in how the dynamics of the impurity particle is affected by the fermion background. To this end, it is instructive to calculate angular momentum carried by the impurity L_1 and the related effective mass. As the impurity is interacting with the fermions, this effective mass is not

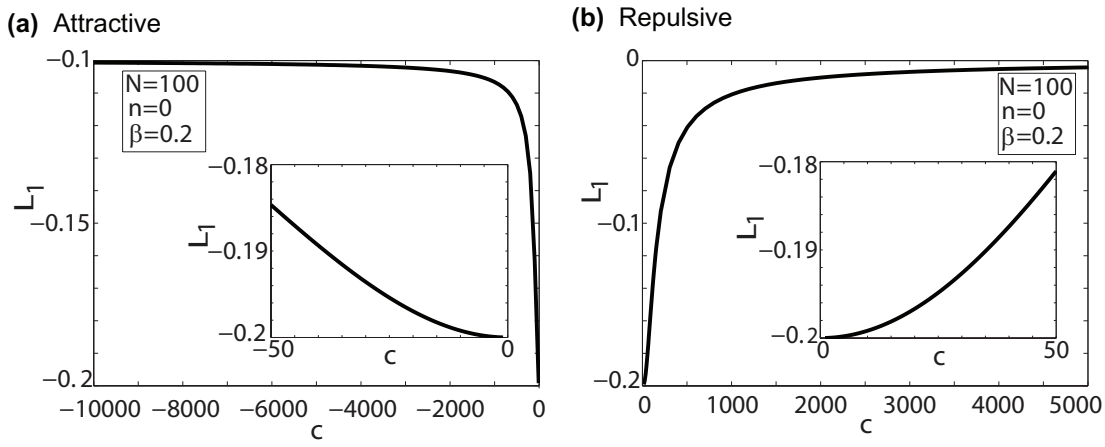

Figure 2.6: Angular momentum of the impurity vs. interaction strength for $N = 100$ particles for (a) attractive and (b) repulsive interactions from the analytic calculation; numerical solutions produce the same results. In the non-interacting limit, the impurity carries all the angular momentum $(n - \beta)$. L_1 saturates to zero for infinitely strong repulsive interactions as the total angular momentum is shared equally between all particles. The same behavior holds for excited states. For strongly attractive interactions, L_1 saturates to half the total value, signifying dimer formation with one background particle. The insets in both figures focus on the weak interaction limit. ©2015 APS

only the mass of the impurity, but, also gets a contribution from the fermions dragged along with it. Such a compound object is generally called the polaron state or dimer state especially for attractive interactions.

As stated above, one of the most physically interesting quantities in this system is the angular momentum carried by the charged particle, represented by the operator $\hat{P}_1 = -i\frac{\partial}{\partial x_1}$. As this particle is coupled to the external magnetic field, $\hat{P}_1$ is the canonical momentum not the kinetic momentum. However, canonical momentum is the quantity that is generally measured by expansion imaging in AMF experiments in cold atoms. The expectation value of $\langle \hat{P}_1 \rangle = L_1$ is easily obtained by taking the derivative of the total energy with respect to flux,

$$L_1 = \frac{-1}{2} \frac{\partial \Delta E}{\partial \beta}. \tag{2.36}$$

Using the approximate form for the energy Eq.2.34, we obtain

$$L_1 = \frac{\pi(n-\beta)}{\text{atan}x_F} - \frac{c}{4\text{atan}x_F}\Big\{(x_F+b)\text{atan}(x_F+b) - (x_F-b)\text{atan}(x_F-b)\Big\}. \tag{2.37}$$

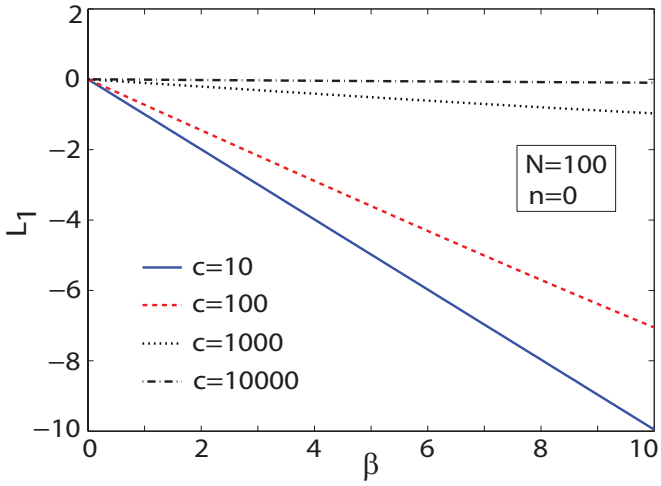

Figure 2.7: The angular momentum of the charged particle vs. flux at varying interaction strength for $N = 100$ particles. As expected L_1 depends linearly on flux. The slope of the line decreases with increasing interaction strength indicating higher values of effective mass of the impurity. ©2015 APS

This form is valid for positive c and easy to interpret. In the non-interacting limit, the canonical momentum of the charged particle is fixed by the external flux. Hence, all the angular momentum is carried by the charged particle. As interactions are turned on, the charged particle drags the background fermions and transfers some of its angular momentum to them. Stronger interactions increase the fraction of the transferred angular momentum, and in the limit of infinitely repulsive interactions, angular momentum is equally shared by N particles. On the other hand, for strong attractive interactions, L_1 saturates to half of the angular momentum in the system proving the formation of a dimer with one background fermion.

The behavior of L_1 is displayed in Fig.2.6 and Fig.2.7 as a function of interaction strength c and flux β. Even for $N = 100$ particles, the difference between numerical calculation of the derivative and the expression given above is negligible. As a function of interaction strength, the rapid decrease and eventual saturation of L_1 validates the scenario discussed above. The linear dependence on flux is expected, however, the slope of L_1 decreases as interaction gets stronger. This slope carries valuable information as it is related to the effective mass of the composite excitation formed by the impurity and background fermions.

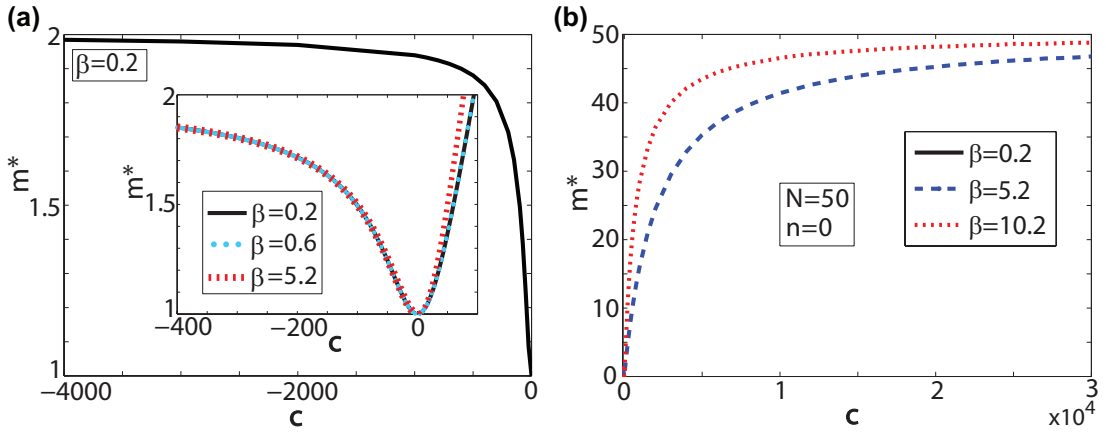

Figure 2.8: Effective mass of the impurity vs. interaction strength for $N = 50$ particles and zero total angular momentum $n = 0$. (a) For attractive interactions, m^* saturates to twice the mass of the impurity due to the formation of a tightly bound pair. The inset shows the behavior around zero interaction in more detail. For attractive interactions, the effective mass (given by Eq.2.39) is almost insensitive to flux change. (b) For repulsive interactions, m^* converges to N. As flux β increases, this saturation gets faster. The dependence on the flux is more prominent for small particle numbers. ©2015 APS

2.3.3 Effective Mass

We define the effective mass as

$$\frac{1}{m^*} = \frac{1}{2}\frac{\partial^2 \Delta E}{\partial \beta^2}. \tag{2.38}$$

In the non-interacting limit, the effective mass is equal to m, however, its behavior is very different for attractive and repulsive interactions. As repulsive interactions are increased, it gets harder for the impurity to tunnel through the fermions and the dragged particles increase the effective mass. The increase in the effective mass saturates only when all the particles are moving together with the impurity. Thus, at large repulsive interaction, the effective mass reaches Nm. For weak attractive interactions, the first effect is once again the drag increasing the effective mass. However, the attractive δ-function has a single bound state in one dimension. Thus, the impurity captures one of the background fermions and as the size of the bound state gets smaller, Pauli exclusion effectively repels the other fermions. The effective mass for attractive interactions increases and reaches $2m$ for infinitely attractive interaction where a dimer is formed from the

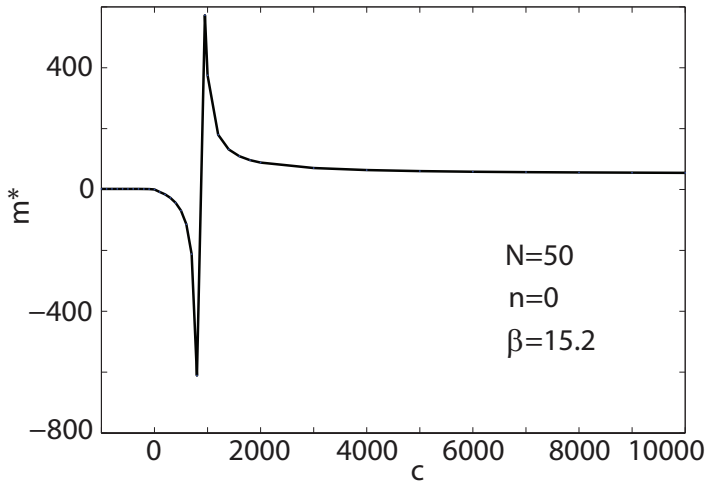

Figure 2.9: Resonant behavior in m^* for β comparable to N. When the dragging effect of the background particles overcomes the driving force of the magnetic field, m^* can become negative. When the second derivative of the energy with respect to flux becomes zero, m^* diverges. This divergence does not alter the infinitely-strong interaction limit. ©2015 APS

impurity and one fermion. For attractive interactions, the analytical expression in the strongly interacting limit is useful to calculate the dimer mass,

$$\begin{aligned}\frac{\partial^2 \Delta E}{\partial \beta^2} = & \frac{2}{1-\frac{\operatorname{atan}(x_F)}{\pi}} - \frac{1}{(1-\frac{\operatorname{atan}(x_F)}{\pi})^2} \\ & + \frac{1}{2\pi(1-\frac{\operatorname{atan}(x_F)}{\pi})^2}\Big\{\operatorname{atan}(x_F+b)+\operatorname{atan}(x_F-b) \\ & + \frac{x_F+b}{1+(x_F+b)^2} + \frac{x_F-b}{1+(x_F-b)^2}\Big\}. \end{aligned} \tag{2.39}$$

We calculated the effective mass numerically and analytically. For the ground state, the above scenario is validated by these calculations (see Fig.2.8). The dependence of the effective mass on the external magnetic field is strongest for small particle number as this limit is the strongly interacting limit in one dimension. As the number of fermions increases, effective mass in the ground state has weak dependence on β. In this case, effective mass is essentially determined locally as the ability for the impurity particle to complete a full rotation is hampered.

The utility of an external magnetic field is the access it provides to excited states through adiabatic pumping. Excited states in this system are expected

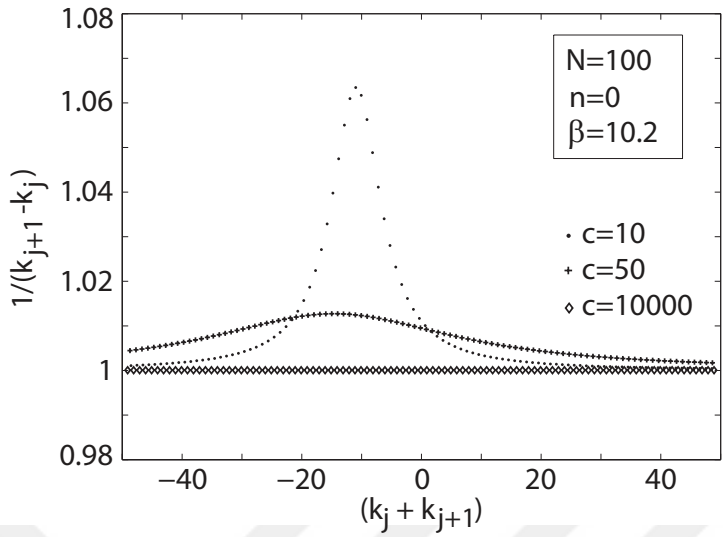

Figure 2.10: Effective momentum density in k-space for different interaction strengths. In the strongly interacting limit, the distance between adjacent BA roots (wavevectors) is one. For small c, the roots are closer to each other around $(n - \beta)$, which means the impurity carrying $n - \beta$ units of angular momentum in the non-interacting limit first disturbs the fermions which are momentum matched to that value. ©2015 APS

to be stable due to angular momentum conservation. It is thus reasonable to expect effective mass measurements to be carried out on such states in a cold atom setting. For the excited states, with angular momentum $|n| < N/4$ the main effect is faster saturation of effective mass as c increases. However, for higher excited states, there is resonant behavior (Fig.2.9). Due to the nature of BA solution, a state for which all the roots are on the *cot* branches from $-N/2$ to $N/2$ can have at most $N/2$ units of angular momentum. When the total angular momentum of an excited state is comparable to particle number N, the sharing of this angular momentum between the impurity and the background is limited by this constraint. Thus, it is possible for this system to support negative effective mass if the external force acted by the magnetic field is overcome by the back reaction from the fermions. We numerically find this behavior for both low and high particle number (see Fig.2.9). Experimentally this effect should be more accessible for small number of particles as it is easier to pump angular momentum comparable to particle number.

2.3.4 Correlations

Apart from the single particle properties related to the impurity, it is instructive to look at global properties to understand how the external particle disturbs the one dimensional Fermi liquid. A common way to visualize the disturbance in the Fermi sea is to plot the deviation of the distance between the BA roots (wavevectors) from one. For an undisturbed Fermi sea, this deviation is always one. For a weakly interacting impurity, the deviation is confined to a narrow region in k-space around $n-\beta$ (see Fig.2.10). This is expected as the impurity carrying $n-\beta$ units of angular momentum in the non-interacting limit first starts dragging fermions which are matched in momentum. As the strength of repulsion increases, so does the effected region in k-space, however, the deviation gets smaller. For infinitely repulsive interactions, the impurity becomes indistinguishable from the background fermions (Fig.2.10). For highly excited states where n is comparable to N, particle-hole excitations complicate this picture similar to the effect we discussed for the effective mass.

Another important physical property is the two-particle correlation function. Although for δ-function interactions only the value of this function at zero determines the interaction energy, its general form is experimentally accessible through Hanbury-Brown-Twiss[58] type measurements. This correlation also can be regarded as the real-space form of the bound state created by the impurity. To calculate the two-particle correlation function, we need to determine the coefficients of the plane waves in each region. Following McGuire [39] we choose the first coefficient in the first region $x_1 < x_2 < \ldots < x_N$,

$$(123..N)_{123..N} = (1 - e^{i2\pi k_1}). \tag{2.40}$$

Other coefficients in this region determined by BCs yield very similar expressions. The wavenumber associated with the distinguishable particle appears in the exponent and the sign of the permutation multiplies the coefficient:

$$\begin{aligned} (213..N)_{123..N} &= -(1 - e^{i2\pi k_2}), & (2.41)\\ (312..N)_{123..N} &= (1 - e^{i2\pi k_3}) & (2.42)\\ &\vdots \end{aligned}$$

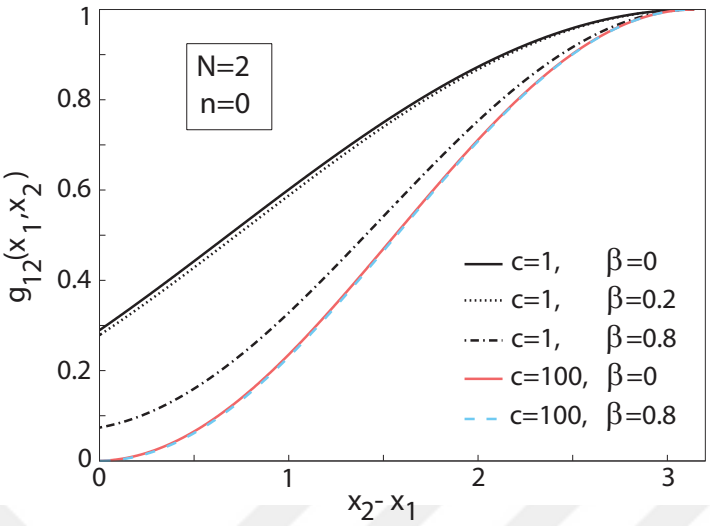

Figure 2.11: Two-particle correlation function for $N = 2$ particles. As expected, g_{12} at zero separation decreases with increasing interaction strength. For weak interactions, the correlation function at zero decreases with increasing flux. However, for strong interactions, the correlation is almost insensitive to flux change due to the fermionization of the charged particle. ©2015 APS

The coefficients in other regions are related to the same coefficient in the first region with a phase factor determined by the PBCs. This phase factor is a full circle rotation around the ring of the particles that x_1 has to pass to be in the given region. Thus, the momenta belonging to the particles that x_1 has passed multiply the coefficient, e.g.

$$(21354..N)_{2314..N} = (1 - e^{i2\pi k_2})e^{i2\pi(k_1+k_3)} \dots \tag{2.43}$$

In the simple form, the wave functions are not normalized, but we normalize the correlation function at the end. The two-particle correlation function in any state is given as

$$g_{12}(x_1, x_2) = \int_0^{2\pi} \mathrm{d}x_3 \cdots \int_0^{2\pi} \mathrm{d}x_N \Psi^* \Psi. \tag{2.44}$$

For the $N = 2$ particle case, the correlation function is simply the absolute square of the wave function. As could be expected, the correlation function is highly affected by the flux for the two-particle case. Using the numerically and

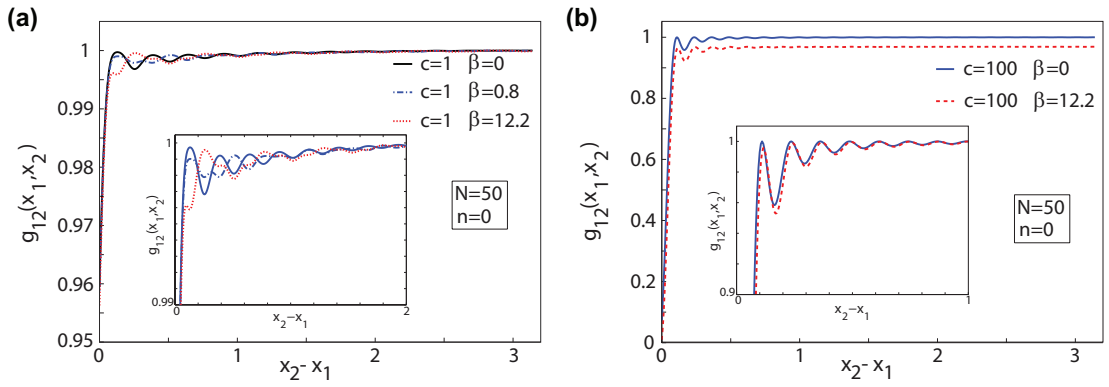

Figure 2.12: Two-particle correlation function for $N = 50$ particles. (a) For weak interactions, Friedel oscillations occur as interference of two waves with wavelengths related to $k_F - \beta$ and $k_F + \beta$. (b) At strong interactions, the correlation becomes zero at zero separation since the impurity is effectively indistinguishable and g_{12} and the frequency of Friedel oscillations are almost insensitive to flux change. ©2015 APS

analytically calculated wavenumbers in the expression,

$$g_{12}(x_1, x_2) = 4 - 2\cos(2\pi k_1) - 2\cos(2\pi k_2) \\ - 8\sin(\pi k_1)\sin(\pi k_2)\cos(k_1 - k_2)(x_2 - x_1 - \pi), \tag{2.45}$$

we observe that inclusion of the flux generally decreases the two-particle correlation function (Fig.2.11). However, if the interactions are strong enough so that the particles are almost fermionized, this decrease is very small. It is also notable that although the flux breaks time-reversal symmetry and the wave functions choose a direction on the ring, correlation function is even with respect to $x_1 - x_2$. This property holds for any particle number.

For the general N particle case, we arrange the wave function in a better form to evaluate the integrals. We assign two wavenumbers to x_1 and x_2, and the rest of the particles are represented by a Slater determinant since they are indistinguishable fermions. For example, if we have k_1, k_4 associated with x_1, x_2 respectively, the Slater determinant is represented by $\mathbb{D}_{14}$ indicating the use of

all wavenumbers except k_1 and k_4 in the exponents,

$$\mathbb{D}_{14} = \begin{vmatrix} e^{ik_2x_3} & e^{ik_3x_3} & e^{ik_5x_3} & \dots \\ e^{ik_2x_4} & e^{ik_3x_4} & e^{ik_5x_4} & \dots \\ \vdots & & & \\ e^{ik_2x_N} & e^{ik_3x_N} & e^{ik_5x_N} & \dots \end{vmatrix}. \tag{2.46}$$

Hence, the wave function in the first region can be written as,

$$\begin{aligned} \Psi =& \Big((12\dots N)_{12\dots N} + (21\dots N)_{12\dots N}\Big)\mathbb{D}_{12} \\ &+ \Big((13\dots N)_{12\dots N} + (31\dots N)_{12\dots N}\Big)\mathbb{D}_{13} + \dots \end{aligned} \tag{2.47}$$

Integrating $\Psi^*\Psi$ over $x_3, \dots, x_N$, the Slater determinants are orthogonal in large particle number limit, as the outer roots of *cot*'s are very close to integer values. The correlation function is then expressed as a sum over pairs of momenta associated with x_1 and x_2,

$$\begin{aligned} g_{12}(x) =& \sum_{t<s}^{N}\sum^{N} |(ts\dots N)|^2 + |(st\dots N)|^2 \\ &+ 2Re\Big\{(ts\dots N)^*(st\dots N)e^{i(k_t-k_s)x}\Big\}, \end{aligned} \tag{2.48}$$

where $x = x_2 - x_1$. Here, $x > 0$ but the symmetry of the correlation function for $x < 0$ can be easily seen by using the region $x_2 < x_3 \dots x_N < x_1$ instead of the first region. Finally, the correlation function is normalized to average density on the ring so that it saturates to one. The correlation function for $N = 2$ and $N = 50$ particles are given in Fig.2.11 and Fig.2.12 respectively, for different interaction strengths and flux. As expected, the correlation function at zero separation $g_{12}(0)$ decreases with increasing interaction strength until it saturates to zero. The other important feature of the correlation function is the Friedel oscillations [59] reflecting the sharpness of the Fermi surface in one dimension.

The two-particle correlation function is a local quantity while the external flux changes the system properties globally. For any pair to feel the effect of the flux,

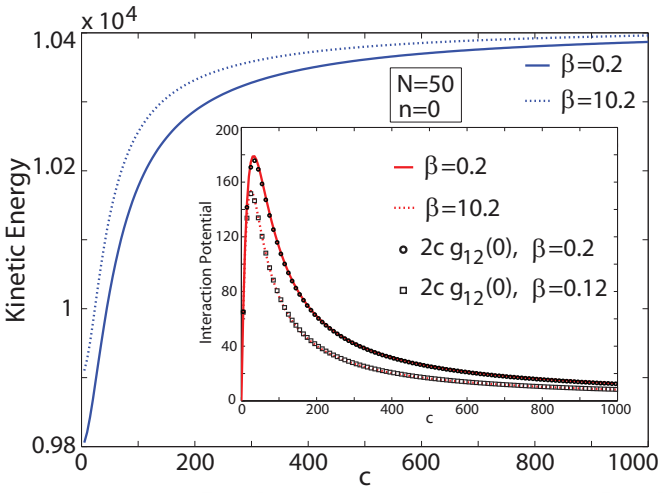

Figure 2.13: Kinetic energy of the particles vs. interaction strength for $\beta = 0.2$ and $\beta = 10.2$ for $N = 50$ particles. The inset shows the interaction potential contribution to the total energy. The initial increase in interaction energy follows the increase in the interaction strength. However, beyond a certain strength, the tendency of the fermions to avoid the impurity is more dominant. These plots are obtained by taking the derivative of the total energy with respect to c. Alternatively, the interaction potential energy is also obtained by using the two-particle correlation function at zero separation. Both results are plotted in the inset showing remarkable agreement. ©2015 APS

one of the particles must go a full circle around the ring. Hence, as could be expected, the effect of the magnetic field on the correlation function decreases as the number of particles increases or if they interact strongly. Even for the lowest lying excited states, we find the primary effect of the flux is on the Friedel oscillations while the shape of the correlation hole is unchanged.

Finally, we calculate a thermodynamic quantity which is also related to $g_{12}(0)$. Derivative of the energy with respect to interaction strength c gives us interaction potential, so, the kinetic and interaction contributions to the total energy can be separated. In Fig.2.13, one can notice that the interaction energy makes a peak and then decreases for increasing c. The initial increase is expected, however, as interactions become stronger, the tendency of the fermions to avoid the impurity dominates and the impurity is effectively fermionized. This is apparent in the δ-function BC Eq.2.8. Additionally, the interaction potential is equal to the correlation function at zero $g_{12}((x_2 - x_1) = 0)$ times the interaction strength

which reproduces the results obtained by taking the derivative of the total energy.

These results show that the system can be described by a simple physical picture. The charged particle interacting with the background particles drags them along with itself around the ring. In the non-interacting limit, all of the angular momentum in the system is carried by the impurity. As interactions are turned on, fermions which are close to the impurity in momentum are disturbed more and start to gain momentum. At the limit of infinitely repulsive interactions, the charged particle is effectively indistinguishable from the background and the total momentum is shared equally between all particles. The pair correlation function also confirms this picture. The value of the correlation function near zero is mostly insensitive to the external flux while away from the correlation hole frequency of the Friedel oscillations sensitively depends on it. For strongly repulsive interactions, the effective mass saturates the total mass of the particles since it is dragging all of the background fermions along with itself around the ring.

For attractive interactions, the impurity forms a bound pair with one of the fermions. The effect of dimer formation can be clearly seen in the angular momentum and the effective mass. For infinitely strong attractive interactions, angular momentum carried by the impurity saturates half the value of total angular momentum and the effective mass saturates twice the mass of the particle which confirm the presence of the dimer as a composite particle.

The physical properties calculated in this chapter are experimentally accessible through the standard tools of ultracold atom experiments. While artificial magnetic fields have been demonstrated in a variety of settings, they have not been used in combination with a toroidal trap to our knowledge. We believe these exact results would be relevant for such an experiment.

Chapter 3

Pairing in the Presence of Change-Imbalance

Superconductivity has attracted great interest since the beginning of 20th century as a demonstration of quantum mechanical effects on macroscopic scales. Although Bardeen-Cooper-Schrieffer (BCS) theory successfully explains superconductor (SC) and superfluid (SF) behavior in a large number of systems [60], there is still much debate over certain limits of SC states, such as the origin of the high-temperature SC [61, 61, 62, 63, 64]. As in many other areas of condensed matter physics, ultracold atomic gases have been used to observe several different aspects of SCs, and the original theories had to be extended to cover these new regimes [7, 8]. Pairing due to resonant interactions has been explored both theoretically and experimentally, uncovering the BEC-BCS crossover in detail. Density imbalance between components forming the Cooper pairs and resulting unconventional SC states were first considered for condensed matter systems, but, experimental observation of polarized SFs [7, 8] with cold atoms required significant improvements upon prior approaches. Similarly, Cooper pairs made up of fermions with unequal masses have been explored theoretically [19, 20], and are yet to be observed experimentally.

The Meissner effect, the expulsion of an external magnetic field from the interior of the sample up to a critical field value H_C, was part of the initial observation regarding the SC states and is one of the most fundamental properties of SCs. Type-II SCs also display a mixed state up to an upper critical field value H_{C2}, where the magnetic field is partially expelled while the material is still electrically superconducting. In this mixed state, the magnetic field penetrates the sample as quantized vortices which then arrange in a lattice (usually in a triangular) formation. This experimentally observed behavior is explained by Abrikosov-Gorkov theory within a semiclassical approximation [65], i.e. the effect of the magnetic field is included only as a phase factor to the wave function. However, it is well known that under a high magnetic field, the energy spectrum of the electrons consists of Landau levels (LLs). This highly-degenerate, discrete spectrum usually results in counterintuitive phenomena as in the case of the quantum Hall effect [66, 67, 68, 69]. One of the mysteries about the SCs is their behavior in this extreme quantum limit.

In the semiclassical regime where the magnetic field is weak, the critical temperature T_C of a SC decreases monotonically with applied field and vanishes at some critical field value H_{C2} (see Fig. 3.1). In 1989, Tešanović et. al predicted that if one includes the LL structure of the electrons, T_C first decreases in the same fashion, but instead of vanishing, starts to increase with some oscillations as demonstrated in Fig. 3.1. The peaks in the density of states reflect onto the phase diagram as oscillations. However, due to the limitations on the magnetic field values that can be created in a solid state system, the high-field phase diagram of SCs is not easy to observe experimentally. Although new developments in experimental techniques constantly push this upper limit up to higher field values, such as the pulsed magnetic fields which can reach up to 100 Tesla [70], observation of the pairing behavior when the particles reside in their first few LLs is still not within the reach of current solid state experiments. One alternative is to use the versatility of the cold atomic gases to observe this quantum limit: AMFs can reach field values much higher than what is attainable in solid state settings. Temperatures and cleanness of the cold atoms would also provide a natural advantage. Since the synthetic gauge fields induce the orbital effect of a

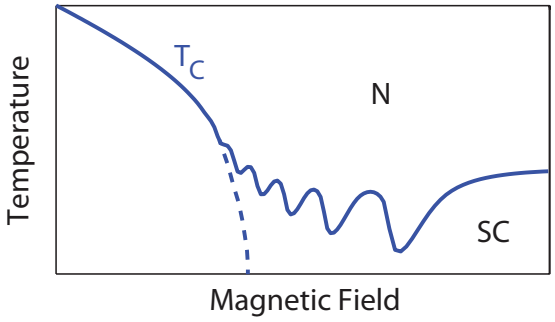

Figure 3.1: Superconducting phase diagram. For weak magnetic fields, semiclassical approximation predicts monotonically decreasing critical temperature T_C (dashed line). For strong magnetic fields, one must consider the Landau level structure. A fully quantum mechanical treatment shows oscillations in T_C at high magnetic fields, corresponding to peak in the density of states.

magnetic field directly into the Hamiltonian, it is possible to isolate the effect of the LL structure on pairing.

Vortex lattices have been already observed in cold atoms by implementing rotation [71, 72, 73]. However, mimicking a magnetic field by physically rotating the gas sets additional constraints on the trapping potential. Although experimentalists have recently succeeded in creating a uniform gas [74], almost all cold atom experiments include a harmonic confinement. In a harmonic trap, if one rotates the gas at a high frequency, the particles would start escaping the confinement, which then hinders the search for high-field superconductivity. Using Raman laser-assisted synthetic gauge fields liberates us from such constraints on the confining potential.

The laser-assisted AMFs are realized by coupling the internal states of the atoms to light to imprint a Berry phase on the motion. While a number of different schemes have been used to manufacture these synthetic Hamiltonians, all of them sensitively depend on the internal excitation structure [11]. Hence, for a mixture of two different atom species or even a mixture composed of atoms in different hyperfine states, the effective magnetic field acting on each component can be different. Although the Zeeman shifts due to the real magnetic field are utilized to create the AMF, this artificial field only couples to the spatial motion of the atoms and does not cause an artificial Zeeman effect [11]. So, we can focus

only on the orbital effect of the magnetic field on SC state.

In this chapter, we explore the consequences of an AMF which couples unequally to the fermions forming a Cooper pair. One can model this system as different effective charges under the same magnetic field (as we implement here), or same charges under different effective magnetic fields. Essentially, we consider the pairing of fermions with different cyclotron frequencies. We discuss the conditions for pairing and the response of the paired state to the external AMF. I will present the two-channel model we use to describe the system in Section 3.1. In Sec. 3.2, I will calculate the gap equation at the transition point. Section 3.3 presents SC phase diagrams for various charge ratios.

Content of this chapter is based on the material published in Ref. [75].

3.1 The Model

We consider a mixture of two fermion species of equal mass and equal density. The system is assumed to be spatially homogeneous, as in most cold atom experiments the effect of the confining potential can be taken into account through the local density approximation. An AMF of arbitrary strength is acting on the system by coupling only to the orbital motion of the fermions, but, causing no Zeeman shift. The coupling of the AMF to each component is different, defining the effective charges q_1 and q_2. Corresponding cyclotron frequencies $\omega_1 = q_1 B/m$ and $\omega_2 = q_2 B/m$ define the respective LL separations. We parameterize the system by using the relative frequency $\omega_r = \omega_2/\omega_1$ and the effective frequency $\omega = \sqrt{\omega_1 \omega_2}$. Within the Landau gauge $\vec{A} = (0, Bx, 0)$, the non-interacting Hamiltonian can be written as

$$\mathcal{H}_0(\omega_1, \omega_2) = \sum_{\nu} \varepsilon_{1\nu} f_{1\nu}^{\dagger} f_{1\nu} + \varepsilon_{2\nu} f_{2\nu}^{\dagger} f_{2\nu}, \tag{3.1}$$

where the subscript $\nu = (n, k_y, k_z)$ incorporates the LL index n, momentum along the z-direction k_z, and the momentum k_y which also labels the LL degeneracy.

The associated kinetic energy for the up and down spin particles is

$$\varepsilon_{i\nu} = \epsilon_{i\nu} - \mu_i = \frac{\hbar^2 k_z^2}{2m} + \hbar\omega_i\Big(n + \frac{1}{2}\Big) - \mu_i, \tag{3.2}$$

for $i = 1, 2$. We fix the total particle number $N = N_1 + N_2$, and consider a mixture of two fermion species of equal mass and density $N_1 = N_2$. The particle number of up and down spins can be written as

$$N_i = \sum_{\substack{k_x,k_y,k_z \\ n}} f(\varepsilon_{i\nu}) = \frac{L_x L_y B}{h/q_i} \sum_{k_z n} f(\varepsilon_{i\nu}) = \frac{L_x L_y L_z B q_i}{(2\pi)^2 \hbar} \sum_n \int_{-\infty}^{\infty} \mathrm{d}\, k_z\, f(\varepsilon_{i\nu}), \tag{3.3}$$

where $V = L_x L_y L_z$ is the volume of the system. The summations over k_x, k_y give the degeneracy of the LLs and $f(\varepsilon_{i\nu})$ is the Fermi-Dirac distribution function,

$$\frac{N_i}{V} = \frac{2}{(2\pi)^2 \ell_i^2} \sum_{n=0}^{\infty} \int_0^{\infty} \mathrm{d}\, k_z \frac{1}{1 + e^{\beta\left(\frac{\hbar^2 k_z^2}{2m} + \hbar\omega_i(n+\frac{1}{2}) - \mu_i\right)}}, \tag{3.4}$$

with $\ell_i = \sqrt{\hbar/m\omega_i}$ being the magnetic length of the particles. The particle densities are then scaled with the effective magnetic length, $\ell = \sqrt{\hbar/m\omega}$, i.e. $n_1 = N_1 2\pi^2 \ell^3/V$. In general, the chemical potentials μ_i are not equal but are chosen to fix the density of both species to be the same at each magnetic field value. We numerically solve the number equations (3.4) for chemical potentials at each AMF value. Thus, for a fixed charge ratio ω_r and total real-space density N/V, changing the AMF strength alters only the effective density n_1.

This single particle spectrum is unique as the LLs of up and down spins do not match in energy. Since their zero point energy and the separation between the LLs are different, two LLs can have equal energy only if the charge ratio ω_r is a rational number. When the chemical potentials are adjusted to equate the densities, low energy single-particle excitation spectra for up and down spins are asymmetric. This mismatch has drastic consequences on pairing when the interactions are introduced.

In a solid state system, the attractive electron-electron interaction in a SC is mediated by the phonons in the system. So, not all of the electrons can interact to form Cooper pairs. The upper limit for phonon energy is given by the Debye frequency [60], and only the electrons in a small region around the Fermi

surface can form pairs. In cold atom experiments, the two species interact resonantly through s-wave scattering. In the absence of phonon energy limiting the electron-electron interaction, one needs alternatives to put a cutoff to the interactions. Here, following Refs.[76, 77] studying the balanced magnetic field case ($\omega_r = 1$), we model the system by using the two-channel Hamiltonian which will intrinsically normalize the interactions. We write the interacting Hamiltonian as

$$\mathcal{H}(\omega_1, \omega_2) = \sum_{\nu} \varepsilon_{1\nu} f_{1\nu}^{\dagger} f_{1\nu} + \varepsilon_{2\nu} f_{2\nu}^{\dagger} f_{2\nu} + \varepsilon_B b^{\dagger} b \ + \alpha \sum_{\nu\nu\prime} Q_{\nu\nu\prime}^{*} b^{\dagger} f_{1\nu} f_{2\nu\prime} + H.c. \tag{3.5}$$

The open-channel fermions interact to form closed-channel bosons with energy

$$\varepsilon_B = \gamma + \frac{\hbar\omega_1 + \hbar\omega_2}{2} - \mu_1 - \mu_2 + C, \tag{3.6}$$

where γ is the unrenormalized detuning between the closed-channel boson and the open-channel fermions. C is the counterterm which will be set to compensate the divergence of the boson self energy due to the infinite number of LLs of the closed-channel fermions. In the original problem, there were only up and down spin fermions interacting through contact interactions. However, we introduced bosons into the system to represent Cooper pairs. The boson energy ε_B and the coupling constant α are not real parameters. The physical parameters are the scattering length and the effective range of the s-wave interactions. So, while using the two-channel model, one needs to relate these secondary parameters to the physical parameters. In the next section, I will present how to perform this renormalization of the two-channel model.

3.1.1 Renormalization of the Two-Channel Hamiltonian

The eigenstates for the open-channel fermions can be written as

$$\psi_{i\nu}(\vec{r}) = \frac{1}{(\pi\ell_i^2)^{1/4}\sqrt{2^n n!}} H_n\Big(\frac{x - x_i}{\ell_i}\Big) e^{-\frac{(x-x_i)^2}{2\ell_i^2}} e^{ik_y y} e^{ik_z z}, \tag{3.7}$$

for $x_i = \hbar k_y / q_i B$ and the n-th Hermite polynomial $H_n(.)$. The closed-channel boson eigenstates $\Phi_{nk_yk_z}$ have the same form as the fermion single particle states,

however the effective charge of the boson is $q_B = q_1 + q_2$, and its mass $2m$. Consequently the boson magnetic length is $\ell_B = \ell_1\ell_2/\sqrt{\ell_1^2+\ell_2^2} = \sqrt{\hbar/m(\omega_1+\omega_2)}$. Two fermions with up and down spin in different LLs can interact to form a boson through the coupling constant α and the overlap integral $Q_{\nu\nu\prime}$. This overlap integral can be calculated by using the eigenstates of the particles,

$$Q_{\nu\nu'} = \int \mathrm{d}^3 r \int \mathrm{d}^3 R\, \psi^*_{1\nu}\Big(\vec{R}+\frac{\vec{r}}{2}\Big)\, \psi^*_{2\nu'}\Big(\vec{R}-\frac{\vec{r}}{2}\Big) D(\vec{r},\vec{R}), \tag{3.8}$$

for the center of mass $\vec{R}$ and relative $\vec{r}$ coordinates of the fermions. We take the wave function of the tightly-bound boson as

$$D(\vec{r},\vec{R}) = \delta(\vec{r}) \sum_p \Phi_{0,p,0}(\vec{R}). \tag{3.9}$$

In general, the sum in Eq. (3.9) should be also over the LL index and momentum along the z-direction for the bosonic wave function. However, the dominant pairing mechanism is through the closed-channel boson with the lowest possible energy. So, we consider coupling of fermions into the bosonic lowest LL (LLL) with zero momentum along z. Hence, the wave function of the boson is in general only a superposition over the degenerate LLL states with different p. However, a straightforward calculation shows that the distribution of the boson wave function over the degenerate LLL states with different p does not affect the physical properties after the bosons are integrated out [77, 76]. Thus, we calculate the overlap integral only for the LLL state with $p = 0$, which gives

$$Q_{\nu\nu'} = \delta(k_z+k_{z'})\delta(k_y+k_{y'}) \frac{(-1)^n \ell_1^n \ell_2^{n'}}{\sqrt{\sqrt{\pi} 2^{n+n'} n! n'! (\ell_1^2+\ell_2^2)^{n+n'+1/2}}} \times e^{-\frac{k_y^2}{2}(\ell_1^2+\ell_2^2)} H_{n+n'}\Big(k_y\sqrt{\ell_1^2+\ell_2^2}\Big). \tag{3.10}$$

After calculating the overlap integral, we need to normalize the boson energy and connect it to the physical parameters. Renormalization can be performed by solving the two particle problem. We consider the most general wave function

$$|\Psi\rangle = \Big(\sum_{\nu\nu'} A_{\nu\nu'} f^\dagger_{1\nu} f^\dagger_{2\nu'} + B b^\dagger\Big)|0\rangle, \tag{3.11}$$

and insert it into the Schrödinger equation,

$$\mathcal{H}(\omega_1,\omega_2)|\Psi\rangle = E|\Psi\rangle. \tag{3.12}$$

By equating the coefficients of bosons and fermions on two sides, we obtain

$$E - \gamma - C = \alpha^2 \sum_{\nu\nu'} \frac{|Q_{\nu\nu'}|^2}{E - \epsilon_{1\nu} - \epsilon_{2\nu'}}. \tag{3.13}$$

We then insert Eq. (3.10) and take the sums over k_y and k_z after converting them into integrals. This leaves only the summations over the LLs of the fermions,

$$\gamma - E = \frac{\alpha^2\sqrt{m}}{4\pi\hbar} \sum_{nn'} \frac{(n+n')!}{n!n'!} \frac{\ell_1^{2n}\ell_2^{2n'}}{(\ell_1^2+\ell_2^2)^{n+n'+1}} \times \frac{1}{\sqrt{\hbar\omega_1\left(n+\frac{1}{2}\right)+\hbar\omega_2\left(n'+\frac{1}{2}\right)-E}} - C. \tag{3.14}$$

The sum on the righthand side diverges due to the infinite number of LLs. So, C is chosen in such a way to suppress this divergence (by setting $E = 0$),

$$C = \frac{\alpha^2\sqrt{m}}{4\pi\hbar} \sum_{nn'} \frac{(n+n')!}{n!n'!} \frac{\ell_1^{2n}\ell_2^{2n'}}{(\ell_1^2+\ell_2^2)^{n+n'+1}} \frac{1}{\sqrt{\hbar\omega_1\left(n+\frac{1}{2}\right)+\hbar\omega_2\left(n'+\frac{1}{2}\right)}}. \tag{3.15}$$

Since we normalize the boson self energy, we can now connect the two-channel model to the real scattering parameters. The system should produce the low energy scattering properties for $(\omega_1, \omega_2) \to 0$. Taking the limit of Eq. (3.14) gives

$$\gamma - E = \frac{-\alpha^2 m^{3/2}}{4\pi\hbar^3}\sqrt{-E}. \tag{3.16}$$

By comparing this equation with the conventional scattering theory result [77, 78]

$$\sqrt{-E} = \frac{\hbar}{a_s\sqrt{m}} - \frac{r_0\sqrt{m}}{2\hbar}E, \tag{3.17}$$

we find that the renormalization parameters γ and α are related to the physical parameters a_s-*scattering length* and r_0-*effective range* as follows,

$$-\frac{\gamma}{\alpha^2} = \frac{m}{a_s\hbar^2 4\pi}, \qquad \frac{1}{\alpha^2} = -\frac{r_0 m^2}{8\pi\hbar^4}. \tag{3.18}$$

3.2 Gap Equation

We examine this Hamiltonian around the SC transition point to calculate the phase diagram. Following mean-field theory, we introduce the average amplitude

of the bosonic wave function $\Delta = \alpha < b >$, which defines the order parameter in the Ginzburg-Landau theory [79]. Near the SC transition, Δ is small, so we can expand the free energy in powers of Δ. For this purpose, we write the Hamiltonian in terms of Δ,

$$\mathcal{H}(\omega_1, \omega_2) = \sum_{\nu} \varepsilon_{1\nu} f_{1\nu}^{\dagger} f_{1\nu} + \varepsilon_{2\nu} f_{2\nu}^{\dagger} f_{2\nu} + \varepsilon_B \frac{\Delta^2}{\alpha^2} + \sum_{\substack{nn' \\ k_y k_z}} \Delta^* Q_{nn'}^* f_{1n} f_{2n'} + H.c. \tag{3.19}$$

The third term in the Hamiltonian (bosonic term) is already second order in Δ, so it is already in the correct order that we are after. There is no first order correction. Introducing attractive interactions to the system gives rise to a second order correction, because particles are converted into pairs two-by-two. Following the same logic, the next term will be fourth order. For small Δ, we can treat the interaction term H_{int} at the end of the Hamiltonian with perturbation theory. The second order correction to the energy due to this interaction term is given by

$$\Theta_{\nu}^{(2)} = \sum_{\substack{\nu' \\ \nu' \neq \nu}} \frac{|\langle \nu | H_{int} | \nu' e \rangle|^2}{E_{\nu} - E_{\nu'}}, \tag{3.20}$$

for the fermionic states $|.\rangle = |00\rangle, |01\rangle, |10\rangle, |11\rangle$ where we can put at most two fermions in a given state. But, since the fermions are created/annihilated in pairs in H_{int}, the states $|01\rangle, |10\rangle$ do not contribute. We then include the Boltzmann weights $exp\{-\beta(\varepsilon_{1n} + \varepsilon_{2n\prime})\}$ of the states experiencing this correction, for inverse temperature $\beta = 1/k_B T$ and Boltzmann constant k_B. So, we have

$$\Theta^{(2)} = \sum_{\substack{nn\prime \\ k_y k_z}} |\Delta Q_{nn\prime}|^2 \frac{e^{-\beta(\varepsilon_{1n} + \varepsilon_{2n\prime})} - 1}{\varepsilon_{1n} + \varepsilon_{2n\prime}} \frac{1}{z}, \tag{3.21}$$

where $z = \left(e^{-\beta\varepsilon_{1n}} + 1\right)\left(e^{-\beta\varepsilon_{2n\prime}} + 1\right)$ is the partition function. If we combine the second order terms, and with a little bit of arrangement, the free energy can be written as

$$\mathcal{F} = \mathcal{F}_0 + \underbrace{\left\{ \frac{\varepsilon_B}{\alpha^2} - \frac{1}{2} \sum_{\substack{n,n' \\ k_y,k_z}} |Q_{nn'}|^2 \frac{\tanh \frac{\varepsilon_{1n}}{2k_BT} + \tanh \frac{\varepsilon_{2n'}}{2k_BT}}{\varepsilon_{1n} + \varepsilon_{2n'}} \right\}}_{0} |\Delta|^2 + O(|\Delta|^4). \quad (3.22)$$

If the second order term is negative, it means that forming Cooper pairs out of fermions is energetically favorable. And if it is positive, we would not have pairs in the system. Critical temperature for pairing is obtained by setting this coefficient to zero. By substituting Eq. (3.18) for the renormalization parameters, and assuming a wide Feshbach resonance, we obtain the gap equation at transition point

$$-\frac{1}{a_s} = \frac{\hbar^2}{m} \sum_{n,n'}^{\infty} \frac{(n+n')!}{n!n'!} \frac{\ell_1^{2n} \ell_2^{2n'}}{(\ell_1^2 + \ell_2^2)^{n+n'+1}} \times \int_{-\infty}^{\infty} \frac{\mathrm{d}k_z}{2\pi} \left\{ \frac{\tanh \frac{\varepsilon_{1n}}{2k_BT} + \tanh \frac{\varepsilon_{2n'}}{2k_BT}}{\varepsilon_{1n} + \varepsilon_{2n'}} - \frac{2}{\epsilon_{1n} + \epsilon_{2n'}} \right\}. \quad (3.23)$$

Right-hand side of Eq.3.23, the pairing susceptibility, determines the behavior of T_C and can be used to understand the underlying physical picture for its evolution.

3.3 Phase Diagram

For a fix particle number and charge ratio ω_r, we solve Eq.3.23 numerically by calculating the pairing susceptibility for a given value of temperature T and n_1 (namely the magnetic field). Phase diagram of the system is then obtained by comparing this value with $-1/a_s$. For the numerical solution, we scale all energies by the effective magnetic energy $\hbar\omega$. Similarly the dimensionless scattering length is $\tilde{a}_s = a_s(N\pi^2)^{1/3}$. Our equations are symmetric for $\omega_r \to \frac{1}{\omega_r}$ which is equivalent to switching the indices of the components. We checked this symmetry numerically and concentrate on $0 < \omega_r \leq 1$ in the following.

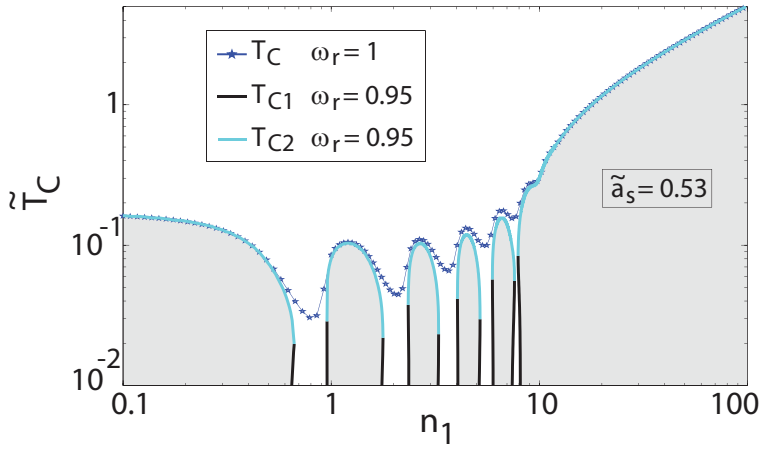

Figure 3.2: Phase diagram of the system as a function of dimensionless temperature $\tilde{T} = k_B T/\hbar\omega$ and effective density $n_1 = N\pi^2\ell^3$ where N is the real-space density and $\ell = \sqrt{\hbar/m\omega}$. Notice that increasing AMF, $B = m\omega/\sqrt{q_1 q_2}$, corresponds to lower n_1 values. Two frequency ratios $\omega_r = 1$ and $\omega_r = 0.95$ are displayed for the same interactions strength $\tilde{a}_s = a_s(N\pi^2)^{1/3} = 0.53$. For $\omega_r = 1$, there is SC transition at any field, the oscillations in T_C (stars) originates from the LL structure. For $\omega_r = 0.95$, this oscillation evolves into bubble SC regions (shaded areas). The system is not SC even at zero temperature between the bubbles and the transition becomes weakly reentrant in temperature. At the low (many LLs) and high field (only LLL) regimes, T_C is not affected significantly by a small charge imbalance. ©2016 APS

In Fig.3.2, we present the phase diagram of $\omega_r = 1$ which is in agreement with Ref. [76]. For the balanced-charge case, there is always a critical temperature below which the SC state is preferred within the mean-field approximation. The critical temperature is non-monotonic with the applied field. It first decreases and becomes exponentially small as smaller number of LLs are involved in the pairing, but, then ultimately increases when only the LLL contributes. This high-field SC has been studied for both solid state [80, 16] and cold atom systems [76]. The oscillatory behavior of T_C with the applied field is a direct result of the underlying LL spectrum. When the LLs of the two components coincide in energy, the pairing susceptibility diverges as $1/\sqrt{T}$ at the peaks and as $\ln(T)$ at the rest in Fig.3.3(a), always guaranteeing a SC state.

We also display the phase diagram for $\omega_r = 0.95$ in Fig.3.2. First of all, unlike the balanced case, there are magnetic field values for which a SC state is never

favored, even at zero temperature. Oscillatory behavior in pairing due to the LL structure causes stable islands of superconductivity in the phase diagram isolated from the zero field SC phase. Although the low field SC is not affected from unequal frequencies, the high-field SC proves to be surprisingly resilient too. The destruction of the low temperature SC in the presence of a small misalignment between LLs has been predicted [81], however, this misalignment also leads to a third effect, reentrant SC. For some AMFs, at low temperatures the sample is in normal state while at higher temperatures it becomes SC. Consequently, even for a slight asymmetry between the charges of the components, the phase diagram undergoes fundamental changes. These changes are most pronounced in the regime where only a few LLs are populated for both components and we display representative phase diagrams in Fig.3.3. In the following, we discuss the physical reason for each of these three features.

Fig.3.3(c) displays the pairing susceptibility for $\omega_r = 0.95$ by focusing on intermediate field strengths. The most striking feature of this phase diagram is the emergence of isolated islands of SC Fig.3.3(d) which come about because Eq.3.23 does not have a solution at some AMF strengths. The absence of solutions even for a minute amount of charge imbalance is best understood by considering the single-particle spectra. The one-particle density of states (DOS) for each component has sharp peaks at each LL threshold. For the balanced case, the DOS and the chemical potentials of the components are always equal. If the temperature is low enough, only the DOS near the chemical potential is relevant. At low temperatures, the pairing susceptibility diverges as $T^{-1/2}$ at each LL threshold and the peaks in T_C follow from the one-particle DOS. When $\omega_r \neq 1$, LLs of different components do not have the same energy or total degeneracy. In general, chemical potentials of both components must be chosen differently to give equal real-space densities. If the mismatch between the chemical potentials and the LLs is large, the energy cost of exciting particles may not be redeemed by attractive interactions even at zero temperature.

The pockets of SC phases roughly correspond to population of a new LL. Whenever a chemical potential crosses a LL threshold, there is a new set of states at the Fermi surface which become suddenly available to contribute to

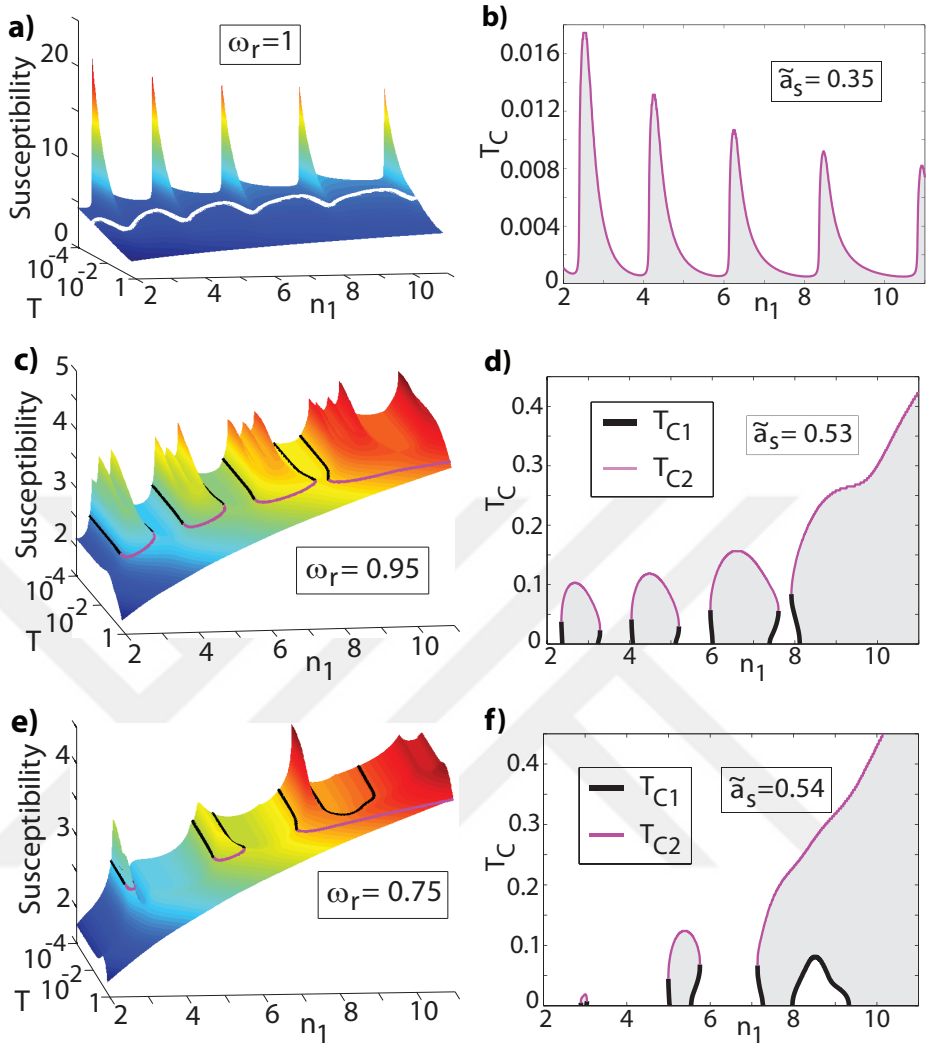

Figure 3.3: Pairing susceptibility (left panel) and respective phase diagrams (right panel) for three frequency ratios $\omega_r = 1, 0.95, 0.75$. The system is made dimensionless with effective magnetic energy $\hbar\omega$ as in Fig.3.2 and decreasing n_1 corresponds to increasing AMF at fixed real-space density N. The phase diagrams are in linear scale in order to cover $T_C = 0$ and plotted for intermediate field strengths where charge imbalance effects are most prominent. a) Pairing susceptibility of equal charges diverges at low temperature, guaranteeing SC for any field value. Divergence is more pronounced at LL thresholds. The corresponding phase diagram (b) is obtained by Eq.3.23. The phase boundary is also highlighted on the surface. c) Even a slight asymmetry between the charges, $\omega_r = 0.95$, lifts the low temperature divergences and the oscillations in (b) turn into bubble SC phases (d). Each LL susceptibility peak is split into smaller peaks, thus, the bubble phases branch into smaller bubbles for weaker interactions (not displayed). e,f) The mismatch between LL spectra is greater for smaller ω_r, resulting in prominent reentrance with temperature. The maximum reentrance temperature is controlled by $\hbar|\omega_1 - \omega_2|$. ©2016 APS

the pairing. The most favorable case for pairing is when both chemical potentials simultaneously cross a new LL. For small charge imbalance, these threshold crossings happen within a small difference in AMF which essentially turns the T_C oscillations of the balanced case into bubble SC phases in Fig.3.3(d). For a general ω_r ratio, the picture is much more complicated. For chemical potentials to give equal densities and cross LL thresholds simultaneously, ω_r must be close to a simple fraction. This complicated behavior is evident in the pairing susceptibilities displayed in Fig.3.3 where simple peaks of balanced LLs are split into smaller structures. For very strong attractive interactions, these bubble phases are not resolved as T_C becomes comparable to the LL separation. A similar effect was predicted for the balanced case [76].

As the magnetic field is increased further, we observe that T_C increases and reaches the same value with the equal charge limit. This surprising revival happens only when both components populate their LLLs. Although the degeneracies of the two LLLs are not equal, they both increase with increasing AMF. The chemical potentials of both components then lie very close to the corresponding LLL thresholds and the asymmetry between the two energy spectra loses its importance. Hence, the excitation cost for pairing decreases at such high fields. We can estimate the AMF for which the effect of charge imbalance vanishes by requiring all the particles with smaller effective charge to reside in their LLL. This estimate is in good agreement with our numerical results.

Another fundamental change brought about by the charge imbalance is SC that is reentrant with temperature. While this effect is not clear for small imbalance as in Fig.3.3(d), we found that it is a common feature of the phase diagrams for general ω_r. A more prominent reentrant SC phase can be observed for $\omega_r = 0.75$ as in Fig.3.3(f). For some field strengths, the system prefers normal phase at zero temperature and becomes SC only above T_{C1}. SC phase subsequently disappears after a higher temperature T_{C2}. Similar reentrant behavior was predicted for graphene bilayers [82] and asymmetric nuclear matter [83]. In our system it is easy to understand the physical basis for this reentrance. Increasing temperature generally prefers a disordered state, however, it also excites a significant amount of particles to higher LLs. Because of the antisymmetric and oscillatory nature of

the DOS in the charge imbalanced system, states which are close to not only the chemical potential but also to LL thresholds are most favorable for pairing. Thus, if the pairing contribution from thermally excited particles overcomes the entropy cost, increasing the temperature can drive the SC transition. With this scenario we expect the maximum lower critical temperature T_{C1} to be of the order of LL mismatch between the components which agrees with our numerical results. In contrast to other reentrant SC phases where a competing order precludes SC at low temperatures [84], the current system has reentrance solely due to non-trivial nature of the single-particle DOS.

Although we concentrate on the interplay between discrete LL structure and charge asymmetry, it is worth mentioning that there is a profound effect even in the semiclassical regime where many LLs are filled for both components. The effect of an external magnetic field on a Cooper pair is modeled by only considering the phase acquired by the center of mass motion. This semiclassical approximation due to orbital dephasing describes the upper critical field H_{C2} in type-II SC successfully. However, if the charges of the fermions forming the pairs are different, the magnetic field couples the center of mass motion with the relative coordinate. As pairing is controlled by the relative coordinate, especially for tightly bound pairs, it is possible for the Lorentz force due to the center of mass motion to break the pairs. Classically, if the center of mass of a bound pair with charges q_1, q_2 is moving with velocity v in a perpendicular magnetic field B, Lorentz force difference between the two particles is $F \simeq |q_1 - q_2|Bv$. This real space picture can be utilized to give a rough estimate for the strength of this pair breaking mechanism by comparing the work done by this force over the size of the pair to the SC gap. This effect becomes dominant especially for large charge ratios and we estimate the upper critical field due to this pair breaking mechanism as $H_{C3} \approx \frac{\sqrt{\omega_r}}{1-\omega_r} H_{C2}$ which is in agreement with our numerical results. While competing orders such as charge density waves, which were not taken into account in our approach, may complicate the physics in the high magnetic field limit, the decease of T_C with charge imbalance is observed even when many LLs are filled and the mean-field approximation is most reliable.

Chapter 4

Non-equilibrium Topological Response

In previous chapters, we have studied different cold atomic systems whose components experience unequal effective magnetic fields under an AMF. Aside from mixtures, developments in AMFs have led to investigation of several other condensed matter phenomena in cold atom experiments, such as the creation and manipulation of topologically protected phases of matter [23, 27, 28, 85, 86].

Topological systems defy Landau theory of phase transitions with information encoded in the global properties of the wave function rather than an energy depending on a local order parameter [13, 87]. Being topologically protected, they exhibit novel quantum phenomena with extreme resilience to local perturbations. The quantum Hall effect (QHE) is an excellent example of topological response as perfectly expressed by Steven Girvin in Poincaré Seminars; "QHE is one of the most remarkable condensed matter phenomena discovered in the second half of the 20th century, rivaling superconductivity in its fundamental significance as a manifestation of quantum mechanics on macroscopic scales" [88]. In QHE, transverse conductance is perfectly quantized with the quantization constant given by the Chern number of the ground state [13, 87] and, hence, cannot be affected by the presence of defects in the sample.

It has been well known that the topological systems are immune to local perturbations for many years, but one important question which naturally arises is the response of a topological system to a global perturbation: What happens if one suddenly changes the Hamiltonian globally or periodically drive the system? While the equilibrium topological properties are studied extensively throughout the literature, these non-equilibrium questions pave the way for new topological phenomena not accessible in conventional equilibrium setups [89, 90, 91, 24, 92, 93, 94, 95]. Effect of a global perturbation on the topological properties, e.g. in the form of a quench, has recently attracted great interest with an ongoing discussion about the characterization of the non-equilibrium topological systems [90, 93]. It has been shown that although the Chern number is preserved following a quench between states with different topology [90, 91], physical observables, like the edge currents, can change depending on the final Hamiltonian not only on the initial state. Hall conductivity is no longer related to the Chern number out-of-equilibrium and, hence, not quantized.

Developments in cold atom experiments have played an important role in these recent theoretical studies on the out-of-equilibrium topological response. It is now within the reach of experiments to change the system parameters faster than the internal dynamics and probe the resulting non-equilibrium system before it decays.

In this chapter, we study non-equilibrium Hall response following a quench where the mass term of a single Dirac cone changes sign. To establish our central result, we first analytically calculate the non-equilibrium response for a single Dirac cone in a two-band model in Sec. 4.1. We then generalize this discussion to the Haldane model in Sec. 4.2, and show that the universal fractional Hall response of a single Dirac cone appears in symmetric quenches of any topological system. We consider both an infinite geometry as well as a strip configuration. The latter configuration lets us study the evolution of the edges modes. In addition to linear response, we explore the full time dynamics of this system in an electric field in Sec. 4.2.2. Then in Sec. 4.2.3, we consider a strip configuration and investigate finite size effects. Section 4.3 focuses on the effect of a harmonic confinement on the Hall conductivity of a strip, and discusses correspondences to

cold atom experiments.

When discussing the neutral atomic systems we will continue to use the language of electrodynamics: The electric field is a force, current is particle current, and the charge is simply unity. Content of this chapter is based on the material published in Ref. [96].

4.1 Single Dirac Cone

Near a topological transition of a $2D$ system, the low-energy physics is described by a massive Dirac model [13, 22, 87]. We parameterize the static Hamiltonian by two quantities; the gap Δ and the 'speed of light' c,

$$\mathcal{H}(\vec{k}) = \begin{pmatrix} \Delta & cke^{i\theta} \\ cke^{-i\theta} & -\Delta \end{pmatrix}, \tag{4.1}$$

where $ke^{i\theta} = k_x + ik_y$ expresses the $2D$ momentum as a complex number. When $\Delta = 0$, the spectrum consists of a gapless Dirac cone at $\vec{k} = 0$. For nonzero Δ, a gap with magnitude $2|\Delta|$ opens at zero momentum. The energies $\varepsilon_n = (-1)^n\sqrt{\Delta^2 + c^2k^2}$ for the band index $n = 1, 2$ are independent of the sign of the gap (mass). The corresponding eigenstates are

$$u_n(\vec{k}) = \frac{1}{N_n(\vec{k})} \begin{pmatrix} (-1)^n cke^{i\theta} \\ \sqrt{\Delta^2 + (ck)^2} - (-1)^n\Delta \end{pmatrix}, \tag{4.2}$$

where $N_n(\vec{k}) = \sqrt{2}\sqrt{\Delta^2 + (ck)^2 - (-1)^n\Delta\sqrt{\Delta^2 + (ck)^2}}$ is the normalization. One imagines that the negative energy modes are filled, and the positive energy modes are empty. The contribution to the Hall conductivity from these low-energy modes can be calculated from the Chern number C via $\sigma_H = Ce^2/h$ [97]. The Chern number is given by

$$C_n = \frac{1}{2\pi}\int d^2k\ \Omega_n(\vec{k}), \tag{4.3}$$

where the Berry curvature is

$$\Omega_n(\vec{k}) = -i\langle\partial_{\vec{k}}u_n(\vec{k})| \times |\partial_{\vec{k}}u_n(\vec{k})\rangle = \frac{(-1)^{n+1}c^2\Delta}{2(\Delta^2 + c^2k^2)^{3/2}}. \tag{4.4}$$

The Berry curvature is odd in the gap parameter, and the Chern numbers of the cones $C = \pm 1/2$ depend on the sign of Δ, even though the energy spectrum does not. The Chern number for a given band must be an integer, so the modes neglected in the low-energy description must also supply a half-integer Chern number. We are envisioning a quench which does not affect these higher energy modes, and their contribution to the Hall conductivity will not change during the quench.

We imagine suddenly flipping the sign of the Δ. The probability $P_n(\vec{k})$ of a particle of momentum k being found in the n^{th} band following this quench is simply the inner product between $u_1(\vec{k})$, and $\bar{u}_n(\vec{k})$, where $\bar{u}_n$ is given by Eq.(4.2) with $\Delta \to -\Delta$. This yields

$$P_1(\vec{k}) = \frac{c^2k^2}{\Delta^2 + c^2k^2}, \quad P_2(\vec{k}) = \frac{\Delta^2}{\Delta^2 + c^2k^2}. \tag{4.5}$$

After the quench, the system is in a non-equilibrium state. Hence, each k point contributes to the Hall conductivity with its Berry curvature weighted by its occupation probability [98, 93],

$$\sigma_{H,neq} = \frac{e^2}{h}C_{neq} = \frac{e^2}{2\pi h}\sum_n \int d^2k P_n(\vec{k})\Omega_n(\vec{k}). \tag{4.6}$$

Any effects from coherences between the bands average out over a time $\tau \sim h/\Delta$, and can be neglected in linear response. Eq.(4.6) reduces to the usual Thouless, Kohmoto, Nightingale and den Nijs (TKNN) formula [97] for the ground state where the occupation probability of the lowest band is one at each k and the higher bands are completely empty. For partially filled bands, the dimensionless Hall conductivity C_{neq} is clearly not quantized and can take any value. However, in a mass-sign-inverting quench, the symmetry between initial and final states will yield a universal result. In particular for our case, the integrals in Eq. (4.6) are elementary and

$$C_{neq} = \frac{1}{3} - \frac{1}{6} = \frac{1}{6}. \tag{4.7}$$

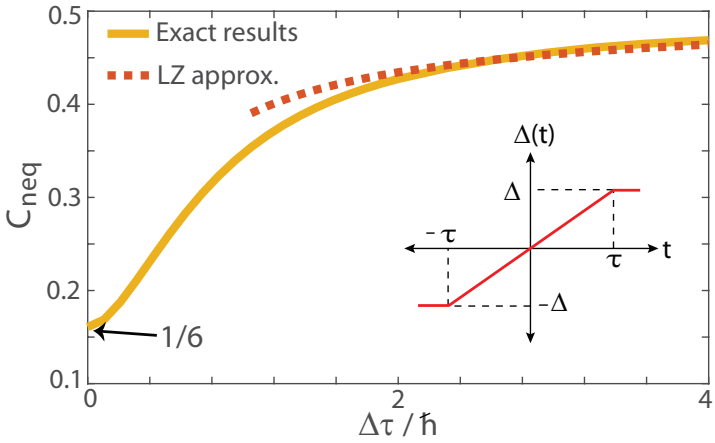

Figure 4.1: Non-equilibrium Hall conductivity, C_{neq}, of a single Dirac cone following a ramp of the gap from $-\Delta$ to Δ in time 2τ as shown in inset. C_{neq} is measured in units of e^2/h, and the product $\Delta\tau/\hbar$ is dimensionless. In the sudden quench limit ($\tau = 0$), $C_{neq} = 1/6$ and as $\Delta\tau \to \infty$, $C_{neq} \to 1/2$. The dashed line shows prediction of the LZ theory from Eq.(4.9). ©2016 APS

Here, the first (second) term is the contribution coming from the lower (upper) band. This fractional Hall response is independent of Δ. Although the Berry curvatures and the number of excited particles are highly sensitive to the value of the gap, they remarkably balance each other in symmetric quenches and one always ends up with 1/6-Hall response. If the quench is performed in the opposite direction, C_{neq} changes sign to $-1/6$. Since the initial Chern number was $\pm 1/2$, the change in the Hall conductivity in such symmetric quenches is always $\pm 2/3$.

For completeness, we also consider sweeps with finite rate where the gap is linearly ramped from $-\Delta$ to Δ within time 2τ as illustrated in the inset of Fig.4.1. We solve the Schrödinger equation

$$i\hbar\frac{\partial}{\partial t}|\Psi(\vec{k},t)\rangle = \mathcal{H}(\vec{k},t)|\Psi(\vec{k},t)\rangle, \tag{4.8}$$

assuming the lower band is initially full. The adiabatic eigenstates of the Hamiltonian traverse an avoided crossing as the sign of the gap changes. At each k, there is an independent Landau-Zener (LZ) problem, with adiabaticity parameter $\eta_k = c^2k^2\tau/\hbar\Delta$. When $\eta_k \gg 1$, the particle remains in the lower band, while $\eta_k \ll 1$ it transitions with the probabilities in Eq.(4.5). Adiabaticity always holds

for modes with sufficiently large k. If the gap is large, $\Delta \gg \hbar/\tau$, then the majority of the modes which contribute to the Hall conductance will be in that region. One can then use the LZ approximation, $P_2(\vec{k},\tau) = e^{-\pi c^2 k^2 \tau/\hbar\Delta}$ which yields a Hall conductivity

$$C_{neq}^{LZ} = -\frac{1}{2} + \pi\sqrt{\frac{\Delta\tau}{\hbar}}e^{\pi\Delta\tau/\hbar}\text{erfc}\left(\sqrt{\pi\frac{\Delta\tau}{\hbar}}\right). \tag{4.9}$$

Here, erfc is the complementary error function. For a general value of $\Delta\tau/\hbar$, we numerically calculate the excitation probabilities and the Hall conductivity (see Fig.4.1). We see that for slow sweeps, the Hall conductivity saturates at $C_{neq} = 1/2$, while rapid quenches yield $C_{neq} = 1/6$. For $\Delta\tau/\hbar > 2$, the Hall conductivity is well approximated by the LZ result Eq.(4.9).

Our result, that the contribution to the non-equilibrium Hall conductivity from a single Dirac cone is 1/6 of the quantum of conductivity, implies that one will see this same fraction in small quenches of any topological lattice system. To illustrate this universality, we study the Haldane model.

4.2 The Haldane Model

4.2.1 Infinite System

The static Haldane Hamiltonian describes non-interacting fermions on a honeycomb lattice (see Fig.4.2(a))

$$\begin{aligned}\mathcal{H} = -t_1 \sum_{<ij>} a_i^\dagger a_j - t_2 \sum_{\ll ij \gg} e^{\pm i\phi} a_i^\dagger a_j \\ + M\sum_A a_i^\dagger a_i - M\sum_B a_i^\dagger a_i,\end{aligned} \tag{4.10}$$

where $a_i^\dagger$ (a_i) creates (annihilates) a fermion at site i. The first term is the nearest-neighbor hopping between the two sublattices, and the second is the next-nearest-neighbor intra-sublattice hopping which breaks time reversal symmetry (TRS).

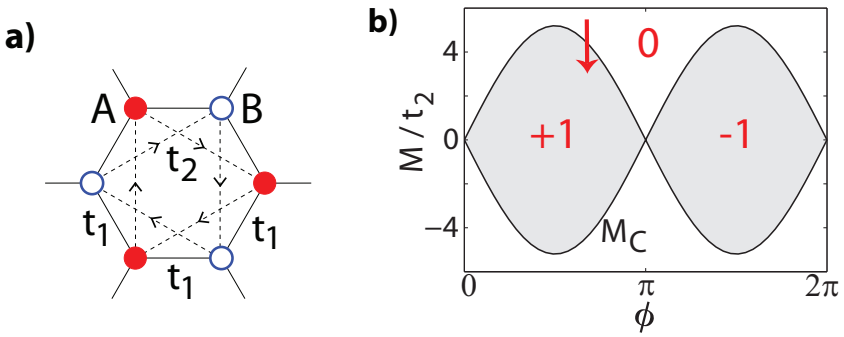

Figure 4.2: Haldane model. (a) illustrates the matrix elements of the tight-binding Hamiltonian in Eq.(4.10); hoppings $t_1, t_2 e^{\pm i\phi}$ and bias $2M$ between A (dark) and B (light) sublattices. (b) Phase diagram showing the Chern number of the lowest band $C = 0, \pm 1$. The arrow indicates the quench studied in the text. Bands touch at a single Dirac point for $M_C = \pm t_2 3\sqrt{3}\sin\phi$. ©2016 APS

The arrows in Fig.4.2(a) represent hopping directions for which the phase gain is positive. An energy offset M of A and B sublattices breaks inversion symmetry (IS). The corresponding phase diagram is given in Fig.4.2(b) where we take $|t_2/t_1| \leq 1/3$ to allow the bands to touch but not to overlap [22]. When both ϕ and M are zero, the spectrum is graphene-like with two Dirac cones in the Brillouin zone. Breaking TRS opens a gap at the two Dirac points, yielding topological bands with Chern numbers $C = \pm 1$. Opening a gap by breaking IS, on the other hand, results in an ordinary insulator (OI) where the Chern numbers vanish. By tuning the competition between the two symmetry breaking terms, one can engineer a topological transition involving only one of the Dirac cones. The critical energy offset of the transition is given by $M_C = \pm t_2 3\sqrt{3}\sin\phi$. The analysis in Section 4.1 suggests that a symmetric quench across this boundary will yield a universal non-equilibrium Hall response.

We now calculate the Hall response of the Haldane model following a quench that changes the mass sign of one of the Dirac cones in the Brillouin zone. As is simplest in experiments, we quench the energy offset M, but a quench of ϕ or t_2 would also work. We start with a completely filled lower band at energy offset $M_i = M_C + \Delta M$ for $\phi = 0.6\pi$ and $t_2 = 0.1 t_1$, where the system is in OI state for $\Delta M > 0$. These lattice parameters are representative: we find equivalent results for other parameters. The first Dirac cone initially contributes a Chern number

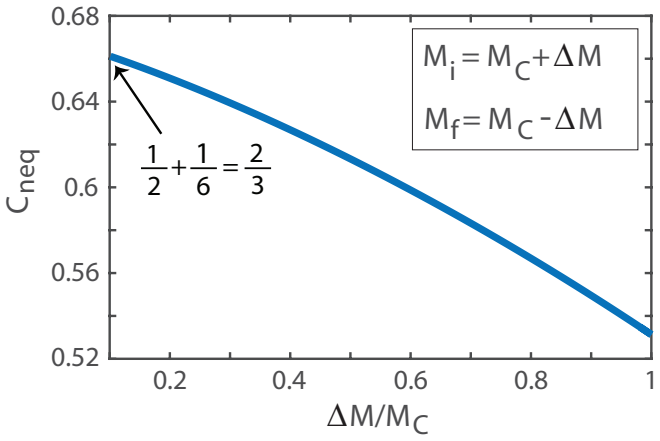

Figure 4.3: Non-equilibrium Hall response of the Haldane model. The energy offset M is suddenly quenched from $M_i = M_C + \Delta M$ to $M_f = M_C - \Delta M$, where $M_C = t_2 3\sqrt{3}\sin\phi$ is the topological transition point. Here $\phi = 0.6\pi$ and $t_2 = 0.1t_1$. For small quenches one reaches the fractional regime in which $C_{neq} \to 2/3$. ©2016 APS

of $-1/2$ where the second one contributes $1/2$, hence the Chern number is zero. We then suddenly change the sublattice bias to $M_f = M_C - \Delta M$, as illustrated in Fig.4.2(b) with the red arrow, and calculate the excitation probabilities at each k in the Brillouin zone. By multiplying the Berry curvatures of the final bands with the occupation probabilities, we calculate the Hall conductivity as in Fig.4.3.

In the limit of $\Delta M \ll M_C$, the transition involves only the first Dirac cone. Since particles near the second Dirac cone are not excited, they continue to contribute $1/2$ to the Chern number. On the other hand, the mass of the first Dirac cone changes sign, so its contribution to the Hall response is $1/6$ as in Sec.4.1. Together they add up to a Hall response of $2/3$, as seen in Fig.4.3. Note that in this limit, the actual number of particles excited to the upper band is small, but the change in the Hall conductivity is still $2/3$ as the Berry curvature is peaked at the Dirac cone. There are no contributions from the rest of the Brillouin zone as the Berry curvature is negligible and no particles are excited. For larger quenches ($\Delta M \sim M_C$), the Hall conductivity deviates from $2/3$ due to the excitations at the second Dirac cone. For quenches in the other direction, from Chern insulator (CI) phase to OI phase, the Hall conductivity becomes $C_{neq} = 1/2 - 1/6 = 1/3$ where the contribution of the first Dirac cone comes with a minus sign.

Experimentally, the local Berry curvature of the bands can be probed by using wave packets [99], which is the measurement of choice in the Zurich experiment [23]. In this method, the wave packet is moved through the Brillouin zone sampling the transverse drift in regions with significant curvature. In quenches on the Haldane model, the action takes place mostly around one of the Dirac cones. If the system is quenched while the wave packet is passing through the Dirac cone of interest, the resulting transverse drift will reveal the contribution of that Dirac cone alone, namely 1/6. Since the observation of the universal 1/6 Hall response does not require a Haldane model, but just the presence of a Dirac cone, it should be also accessible in the hexagonal lattices of the Hamburg [24] and Munich groups [25] as long as one can isolate the contribution of a single Dirac cone. In practice, extracting the Chern number from such experiments requires attention to several technical details [99, 23, 85, 92, 100]. We discuss an alternative approach in Section 4.3.

4.2.2 Beyond Linear Response

In an equilibrium state (at half filling), where the bands are either completely filled or empty, the occupation probability at each point in the Brillouin zone does not change when a force is applied [97]. However, in a non-equilibrium state, the nonuniform distribution will evolve as forces are applied, leading to pronounced nonlinearities in the Hall response. Here we characterize these nonlinearities. Linear response should be valid when the impulse imparted on the atoms $I = E\Delta t$ is small compared to the width of the Dirac cone Δ/c. Here we relax this constraint but still take $E \ll \Delta^2$. In this regime band coherences can be neglected, and one does not encounter the zitterbewegung related effects found in Ref.[92] when they considered delta-function impulses.

An infinitesimal impulse $dI\hat{y}$ shifts a particle in the n^{th} band with a momentum $\vec{k}$ to $\vec{k} + dI\hat{y}$, and shifts its center-of-mass in the transverse direction by $dX = \Omega_n(k)dI$. The total displacement of the cloud is found by adding up the contribution from each (n, k) mode; weighted by the probability of occupation

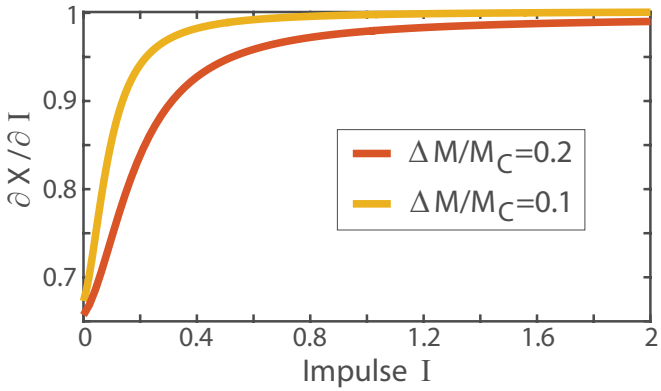

Figure 4.4: Nonlinear Hall response $C_{neq} = \partial X/\partial I$ following a quench, for transverse displacement X resulting from an impulse I. The parameters are adimensionalized by using the unit length of the lattice. The system is quenched between states ΔM around the transition point M_C as detailed in the text. The Hall response of a non-equilibrium system saturates to equilibrium result ($C = 1$ in this case) for large impulse. Linear response regime shrinks for decreasing ΔM. ©2016 APS

$P_n(\vec{k})$. The response to a finite impulse is then calculated by adding up these infinitesimals,

$$X(I) = \frac{1}{2\pi} \int_0^I dI' \sum_n \int_{BZ} d^2k P_n(\vec{k} - I'\hat{y}) \Omega_n(\vec{k}). \tag{4.11}$$

The rate of change of this transverse displacement gives the Hall conductivity $\sigma_H = \partial X/\partial I$.

As in Section 4.2.1, we quench the system from the ground state of the OI phase at $M_i = M_C + \Delta M$ to the CI phase at $M_f = M_C - \Delta M$ (where $C = 1$) with $t_2 = 0.1t_1$ and $\phi = 0.6\pi$. We numerically calculate the final Berry curvatures $\Omega_n(\vec{k})$ and the probability distributions within the bands $P_n(\vec{k})$. We then apply an impulse $I\hat{y}$ which shifts the probability distributions according to Eq.(4.11). As seen in Fig.4.4, the resulting Hall conductivity $\sigma_H = \partial X/\partial I$ depends on the applied impulse.

We observe a crossover from a fractional Hall response to an integer response. For large impulses, the excited particles move away from the Dirac point towards k-values with negligible curvature. The lower band becomes again completely filled around the Dirac cone and the upper band completely empty. Hence, the

Hall response approaches that of the equilibrium system ($C = 1$ in this case). In Fig.4.4, we consider two different values of ΔM. For smaller ΔM, particle excitations and curvature are more confined around the Dirac point, resulting in a smaller linear response regime.

In experiments on equilibrium states, larger impulses are almost always favorable: The bigger the impulse, the larger the transverse drift and hence the larger the signal. In a non-equilibrium setting, however, there is a tension between the desire to have a large signal, and the desire to be in the linear response regime. The strength of the impulse should be chosen carefully.

Up to this point we have been considering an experiment in which the fermionic cloud is initially in its ground state, and hence the Brillouin zone is uniformly filled. One could imagine other scenarios in which this fractional quantized conductance could be explored. For example, one could fill only the states near the Dirac cone (those with $k \lesssim \Delta/c$). In that case, one could observe the 1/6 Hall response of that Dirac cone. Of course, if the spread of the cloud in k-space is too small, or too large, a non-universal value would be found. Many of the Haldane model experiments in Zurich have utilized such partially filled bands [23].

4.2.3 Strip geometry

The energy spectrum of a finite topological system is fundamentally different than the infinite system due to the presence of protected edge modes. In this section, we investigate how edge states modify both the equilibrium, and non-equilibrium Hall response. We find that for wide enough strips, our results from bulk calculations hold. We also set up notation for exploring the spatial distribution of currents in a harmonic trap. In Sec.4.3, we show that these currents can be used as a probe of the Hall effect.

We take the system to be infinite in the x-direction and finite in the y-direction with an armchair termination. We define a 'layer' index for each site, which corresponds to its y-position as shown in Fig.4.5. Under a uniform electric field

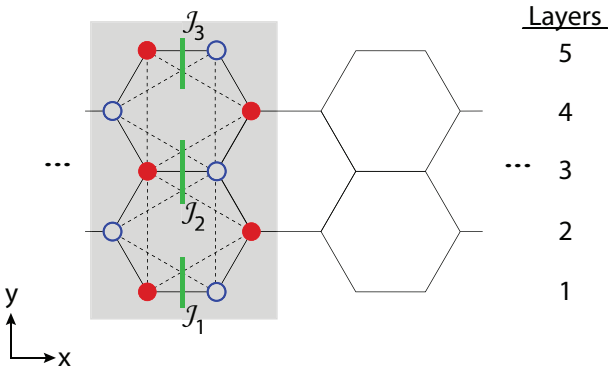

Figure 4.5: Haldane strip with armchair termination, for parameters introduced in Fig.4.2(a). Unit cell is given by the shaded area. We label the layers in the finite y-direction. Green (thick vertical) lines represent how nearest- and next-nearest-neighbor hoppings are assigned into these layers to calculate the current density $\mathcal{J}_\ell$. ©2016 APS

$E\hat{y}$ in the finite direction, a Hall current J_H flows along the strip in the x-direction.

Our Hamiltonian can be expressed as $\mathcal{H} = -\sum_{ij} t_{i\to j} a_i^\dagger a_j + M\sum_A a_i^\dagger a_i - M\sum_B a_i^\dagger a_j$. The matrix element $t_{i\to j}$ is equal to t_1 for neighboring sites, $t_2 e^{\pm i\phi}$ for next-neighbor sites, and 0 for all others. The current from site i to j is then

$$\mathcal{J}_{i\to j} = 2\mathrm{Im}\{t_{j\to i}\langle a_i^\dagger a_j\rangle\}. \tag{4.12}$$

To quantify the spatial distribution of currents, we group the currents according to the layers of i and j. For each odd integer ℓ, we define $\mathcal{J}_\ell$ to be the sum of currents either originating from or ending at the ℓ^{th} layer, at some fixed x-position in the unit cell (see Fig.4.5). In an OI state, $J_H = \sum \mathcal{J}_\ell$ is always zero even though there may be nonzero currents in individual layers. For a CI phase, however, J_H is finite in the presence of a nonzero electric field. The Hall conductivity of the strip is then $\sigma_H^s = \frac{1}{W}\frac{\partial J_H}{\partial E}$ where W is the width of the strip.

Cold atom experiments can explore strips of varying width, even as small as two layers [86]. Thus, they are well suited to quantifying finite size effects. To analyze these effects in accessing bulk topological properties, here we first consider equilibrium Hall response of a strip in CI regime.

We take an L layer strip with $M = 0, t_2 = 0.1t_1$ and $\phi = 0.6\pi$. Here, the

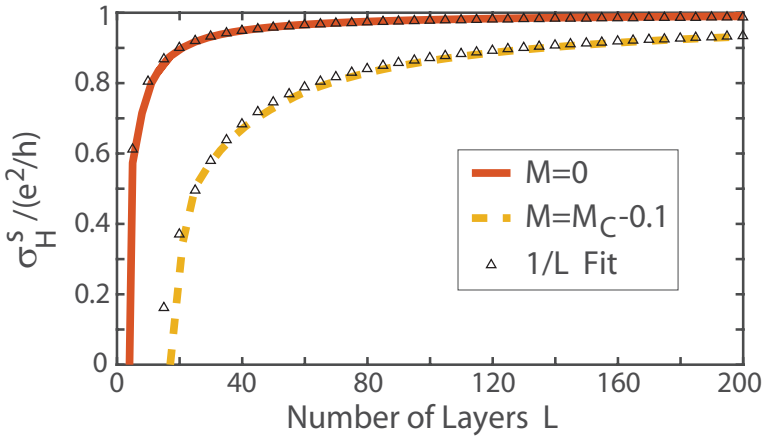

Figure 4.6: Equilibrium Hall conductivity of the strip as a function of number of layers in the finite direction. The system is in CI state at $M = 0$ and $M = M_C - 0.1$, for $t_2 = 0.1t_1$ and $\phi = 0.6\pi$. Hall conductivity approaches to the quantized bulk value as $1/L$ for increasing strip width. ©2016 APS

edge states are well separated from the bulk, and we take the Fermi energy to lie in the bulk gap. An infinite system with these parameters would have a Chern number of 1. We apply an electric field, and measure the resulting J_H. Due to the presence of the hallmark edge states, we find that σ_H is somewhat smaller than one would expect from the bulk calculations (see Fig.4.6). The deviation falls off as $1/L$ for large L. This is sensible, as the ratio of edge to bulk modes falls off with this same power. We repeat this calculation at $M = M_C - 0.1$, where the bulk gap is smaller. Given the larger extent of the edge modes, it is not surprising that we find a larger deviation from bulk behavior.

We now consider a wide strip and study our symmetric quenches of Section 4.2.1. We start with a ground state as before in the OI phase at $M_i = M_C + \Delta M$ with the same parameters in the previous section $t_2 = 0.1t_1$ and $\phi = 0.6\pi$. We numerically calculate the initial eigenstates for $L = 201$ layers. We then quench the system into the CI phase at $M_f = M_C - \Delta M$ and find the occupation probabilities of the final eigenstates by calculating overlaps with the final eigenstates.

To explore the Hall response, we then add a small electric field $E\hat{y}$, and calculate the currents in our non-equilibrium state. We find that for small quenches $\Delta M/M_C = 0.1$ and 0.2, the resulting Hall response of the strip is $\sigma_H^s = 0.66$

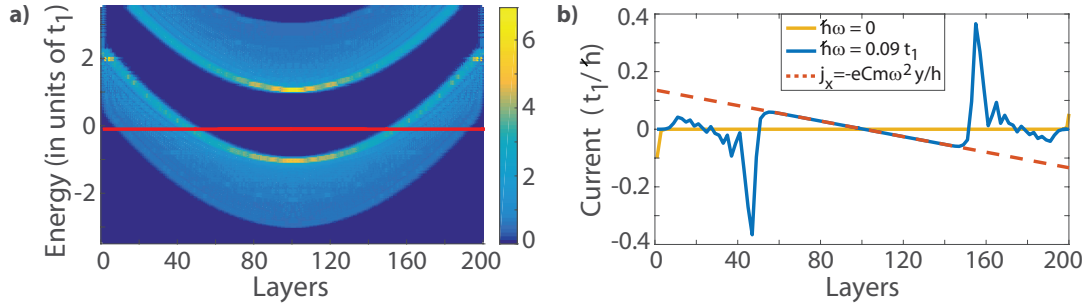

Figure 4.7: Effect of a harmonic trap with $\hbar\omega = 0.09t_1$ in the finite direction for $M = 0$, $t_2 = 0.2t_1$ and $\phi = 0.5\pi$. (a) Local density of states along the finite direction where the center is a CI and the edges are metallic. The Fermi energy is indicated with the red line. (b) Current density flowing along the strip with (dark line) and without (light line) trap, in the absence of an electric field. The force exerted by the trap $F_y = -m\omega^2 y$ results in anomalous currents in the central topological region according to $j_x = eCF_y/h$ (dashed line). ©2016 APS

and 0.65 respectively. Hence, in small quenches symmetric around the transition point, the Hall conductivity of a strip successfully reproduces the infinite system result of 2/3.

4.3 Harmonic Trap

Nearly all cold atom experiments include a harmonic trap. Naively, this potential complicates the search for topological physics: Even if the center of the cloud is a CI, the edge is always metallic. The metallic edges wash out any potential signals from edge modes, and one might expect them to dominate the Hall response, yielding non-universal, non-quantized results. In this section, we investigate a Haldane model with harmonic confinement added. We find equilibrium currents whose spatial distribution reveals the underlying topological physics. We discuss protocols for detecting these currents, and using them to infer the quantize Hall response.

We take the formalism of Section 4.2.3, and add a potential $H = \sum_i \frac{1}{2}m\omega^2 y_i^2$ where y_i is the y-position of the i^{th} site. We consider this uni-directional harmonic

potential as it makes analyzing the currents simpler. In a cylindrically symmetric harmonic trap, one would observe similar results, with the radial direction playing the role of y. In Fig.4.7(a), we show the local density of states of this system, taking $M = 0$, $t_2 = 0.2t_1$, $\phi = 0.5\pi$, and $\hbar\omega = 0.09t_1$. We take the chemical potential to lie in the bulk gap at the center of the cloud, which will locally be in the CI phase. The metallic edges are characterized by the finite density of states at the Fermi level.

In Fig.4.7(b), we show the local equilibrium current $\mathcal{J}_\ell$, as a function of position in finite direction in the absence of an electric field. In the insulating region, one sees a current which grows linearly with position in a trap. On the metallic edges, there are large counter-propagating currents. The net current vanishes. The bulk currents are nothing but the quantized anomalous Hall currents coming from the topological band and the trapping potential. The trap is equivalent to a spatially dependent electric field $E_y = -m\omega^2 y/e$. Within a local density approximation this leads to a local current density $j_x = \sigma_H E_y = -eCm\omega^2 y/h$. Indeed, the slope of the line in Fig.4.7(b) matches this prediction.

We also propose a simple protocol to measure these local currents. One begins with a non-interacting spin polarized Fermi gas in a situation like Fig.4.7(a). Using standard techniques [30, 101, 102, 103], one locally flips the spins of a small number of atoms. Local currents will be apparent in the motions of these spins. Cold atom experiments can explore not only the average current, but also the spatial distribution of the currents [86, 104]. This extra information can disentangle the contributions from the metallic edges and the bulk. Furthermore, if the system is to be quenched, one can still access the Hall response of the topological central region even in the presence of a harmonic trap.

Chapter 5

Conclusion

The experiments of ultracold quantum gases have made a breakthrough with the development of synthetic gauge fields which enable the investigation of orbital magnetism effects in these neutral systems. In this thesis, we tried to show that the specifics of experimental recipes for creating these AMFs can further offer access to hitherto unexplored limits of traditional condensed matter theories and provide us with a deeper understanding of them.

Cold-atom experiments under AMFs can create mixtures where each component experiences a different effective magnetic field. In order to demonstrate the consequences of such unequal coupling to an external magnetic field, we first considered an impurity problem. We argued that an artificial gauge field coupling exclusively to the impurity in a spin-polarized Fermi gas is an effective tool to probe the polaron physics at any interaction strength. We solved this system exactly by using the BA for contact interactions and calculate the dependence of measurable quantities on the external magnetic flux. We observed this dependence for total energy, angular momentum of the charged particle, effective mass and the two-particle correlation function. Using an artificial magnetic field in this system has two advantages. The usual measurement tools such as expansion imaging become probes of thermodynamic quantities by comparing measurements at different flux values. For example, the change of the momentum carried by the

impurity caused by the magnetic field is a direct probe of the effective mass of the impurity. The second advantage is obtained by adiabatically increasing the flux value. Although the Hamiltonian of the system is periodic with flux, adiabatic evolution connects the ground state at zero flux to excited states at integer flux. In a cold atom experiment, such excited states can be expected to have long lifetimes due to total angular momentum conservation. Thus, we have calculated the physical properties for not only the ground state but also for excited states adiabatically connected to it.

Secondly, we examined the pairing behavior between fermions of unequal effective charges which constitutes a unique extension of BCS theory. We have found that even for a slight asymmetry between the single-particle energy spectra of the particles forming the Cooper pairs, the phase diagram changes drastically with the emergence of reentrant SC both in temperature and magnetic field. The oscillatory behavior of T_C with magnetic field for the balanced case modifies into isolated SC phases. For extremely high AMF values where both components are in their LLLs, the transition temperature is independent of the charge ratio.

Finally, we turned our attention to investigation of topologically ordered states of matter in ultracold atomic gases which was rendered possible by implementing AMFs in optical lattices. Extreme controllability of the experiments allows changing the parameters of the Hamiltonian faster than the internal dynamics, providing access to non-equilibrium physics. These out-of-equilibrium systems exhibit new topological phenomena which have no equilibrium counterpart. Here, by considering Chern insulators, we showed a universal fractional value of the Hall conductivity when the mass sign of a single Dirac cone in a two-band model is suddenly changed. The energy spectrum is independent of the sign of the gap while the eigenstates are sensitive to it. We find that this symmetry results in a contribution to the Hall response of $|C_{neq}| = 1/6$ independently from the actual value of the gap. By studying the Haldane model, we illustrate the universality of this result: Any symmetric topological quench dominated by a single Dirac cone will observe this fractional Hall response.

Bibliography

[1] Y.-J. Lin, R. L. Compton, K. Jiménez-Garcia, J. V. Porto, and I. B. Spielman, "Synthetic magnetic fields for ultracold neutral atoms," *Nature*, vol. 462, pp. 628–632, 2009.

[2] M. H. Anderson, J. R. Ensher, M. R. Matthews, C. E. Wieman, and E. A. Cornell, "Observation of Bose-Einstein condensation in a dilute atomic vapor," *Science*, vol. 269, no. 5221, pp. 198–201, 1995.

[3] K. B. Davis, M. O. Mewes, M. R. Andrews, N. J. van Druten, D. S. Durfee, D. M. Kurn, and W. Ketterle, "Bose-Einstein condensation in a gas of sodium atoms," *Phys. Rev. Lett.*, vol. 75, pp. 3969–3973, Nov 1995.

[4] R. P. Feynman, "Simulating physics with computers," *Int. J. Theor. Phys.*, vol. 21, p. 467, 1982.

[5] M. Greiner, C. A. Regal, and D. S. Jin, "Emergence of a molecular Bose-Einstein condensate from a Fermi gas," *Nature*, vol. 426, pp. 537–540, 2003.

[6] M. Greiner, O. Mandel, T. Esslinger, T. W. Hänsch, and I. Bloch, "Quantum phase transition from a superfluid to a Mott insulator in a gas of ultracold atoms," *Nature*, vol. 415, pp. 39–44, 2002.

[7] M. W. Zwierlein, A. Schirotzek, C. H. Schunck, and W. Ketterle, "Fermionic superfluidity with imbalanced spin populations," *Science*, vol. 311, no. 5760, pp. 492–496, 2006.

[8] G. B. Partridge, W. Li, R. I. Kamar, Y.-A. Liao, and R. G. Hulet, "Pairing and phase separation in a polarized Fermi gas," *Science*, vol. 311, no. 5760, pp. 503–505, 2006.

[9] C. Chin, R. Grimm, P. Julienne, and E. Tiesinga, "Feshbach resonances in ultracold gases," *Rev. Mod. Phys.*, vol. 82, pp. 1225–1286, Apr 2010.

[10] N. Cooper, "Rapidly rotating atomic gases," *Advances in Physics*, vol. 57, no. 6, pp. 539–616, 2008.

[11] J. Dalibard, F. Gerbier, G. Juzeliūnas, and P. Öhberg, "*Colloquium* : Artificial gauge potentials for neutral atoms," *Rev. Mod. Phys.*, vol. 83, pp. 1523–1543, Nov 2011.

[12] N. Goldman, G. Juzeliunas, P. hberg, and I. B. Spielman, "Light-induced gauge fields for ultracold atoms," *Reports on Progress in Physics*, vol. 77, no. 12, p. 126401, 2014.

[13] D. Xiao, M.-C. Chang, and Q. Niu, "Berry phase effects on electronic properties," *Rev. Mod. Phys.*, vol. 82, pp. 1959–2007, Jul 2010.

[14] M. Mancini, G. Pagano, G. Cappellini, L. Livi, M. Rider, J. Catani, C. Sias, P. Zoller, M. Inguscio, M. Dalmonte, and L. Fallani, "Observation of chiral edge states with neutral fermions in synthetic Hall ribbons," *Science*, vol. 349, no. 6255, pp. 1510–1513, 2015.

[15] B. K. Stuhl, H.-I. Lu, L. M. Aycock, D. Genkina, and I. B. Spielman, "Visualizing edge states with an atomic Bose gas in the quantum Hall regime," *Science*, vol. 349, no. 6255, pp. 1514–1518, 2015.

[16] Z. Tešanović, M. Rasolt, and L. Xing, "Quantum limit of a flux lattice: Superconductivity and magnetic field in a new relationship," *Phys. Rev. Lett.*, vol. 63, pp. 2425–2428, Nov 1989.

[17] P. Fulde and R. A. Ferrell, "Superconductivity in a strong spin-exchange field," *Phys. Rev.*, vol. 135, pp. A550–A563, Aug 1964.

[18] A. I. Larkin and Y. N. Ovchinnikov, "Inhomogeneous state of superconductors," *Sov. Phys. JETP*, vol. 20, p. 762, 1965.

[19] W. V. Liu and F. Wilczek, "Interior gap superfluidity," *Phys. Rev. Lett.*, vol. 90, p. 047002, Jan 2003.

[20] P. F. Bedaque, H. Caldas, and G. Rupak, "Phase separation in asymmetrical fermion superfluids," *Phys. Rev. Lett.*, vol. 91, p. 247002, Dec 2003.

[21] E. Gibney and D. Castelvecchi, "Physics of 2D exotic matter wins nobel," *Nature*, vol. 538, p. 18, 2016.

[22] F. D. M. Haldane, "Model for a quantum Hall effect without Landau levels: Condensed-matter realization of the "parity anomaly"," *Phys. Rev. Lett.*, vol. 61, pp. 2015–2018, Oct 1988.

[23] G. Jotzu, M. Messer, R. Desbuquois, M. Lebrat, T. Uehlinger, D. Greif, and T. Esslinger, "Experimental realization of the topological Haldane model with ultracold fermions," *Nature*, vol. 515, p. 237, 2014.

[24] N. Fläschner, D. Vogel, M. Tarnowski, B. S. Rem, D.-S. Lhmann, M. Heyl, J. C. Budich, L. Mathey, K. Sengstock, and C. Weitenberg, "Observation of a dynamical topological phase transition," *arXiv:1608.05616*, 2016.

[25] L. Duca, T. Li, M. Reitter, I. Bloch, M. Schleier-Smith, and U. Schneider, "An Aharonov-Bohm interferometer for determining Bloch band topology," *Science*, vol. 347, no. 6219, pp. 288–292, 2015.

[26] N. Goldman, J. C. Budich, and P. Zoller, "Topological quantum matter with ultracold gases in optical lattices," *Nature Physics*, vol. 12, p. 639, 2016.

[27] L. Tarruell, D. Greif, T. Uehlinger, G. Jotzu, and T. Esslinger, "Creating, moving and merging Dirac points with a Fermi gas in a tunable honeycomb lattice," *Nature*, vol. 483, pp. 302–305, 2012.

[28] T. Uehlinger, G. Jotzu, M. Messer, D. Greif, W. Hofstetter, U. Bissbort, and T. Esslinger, "Artificial graphene with tunable interactions," *Phys. Rev. Lett.*, vol. 111, p. 185307, Oct 2013.

[29] J. Kondo, "Resistance minimum in dilute magnetic alloys," *Progress of Theoretical Physics*, vol. 32, no. 1, pp. 37–49, 1964.

[30] T. Fukuhara, A. Kantian, M. Endres, M. Cheneau, P. Schau, S. Hild, D. Bellem, U. Schollwck, T. Giamarchi, C. Gross, I. Bloch, and S. Kuhr, "Quantum dynamics of a mobile spin impurity," *Nature*, vol. 9, pp. 235–241, 2013.

[31] A. Kantian, U. Schollwöck, and T. Giamarchi, "Competing regimes of motion of 1D mobile impurities," *Phys. Rev. Lett.*, vol. 113, p. 070601, Aug 2014.

[32] S. Palzer, C. Zipkes, C. Sias, and M. Köhl, "Quantum transport through a Tonks-Girardeau gas," *Phys. Rev. Lett.*, vol. 103, p. 150601, Oct 2009.

[33] M. B. Zvonarev, V. V. Cheianov, and T. Giamarchi, "Spin dynamics in a one-dimensional ferromagnetic Bose gas," *Phys. Rev. Lett.*, vol. 99, p. 240404, Dec 2007.

[34] A. J. Leggett, S. Chakravarty, A. T. Dorsey, M. P. A. Fisher, A. Garg, and W. Zwerger, "Dynamics of the dissipative two-state system," *Rev. Mod. Phys.*, vol. 59, pp. 1–85, Jan 1987.

[35] F. Grusdt and E. Demler, "New theoretical approaches to Bose polarons," *arXiv:1510.04934*, 2015.

[36] H. Bethe, "Zur theorie der metalle," *Zeitschrift für Physik*, vol. 71, no. 3-4, pp. 205–226, 1931.

[37] E. H. Lieb and W. Liniger, "Exact analysis of an interacting Bose gas. i. The general solution and the ground state," *Phys. Rev.*, vol. 130, pp. 1605–1616, May 1963.

[38] C. N. Yang, "Some exact results for the many-body problem in one dimension with repulsive delta-function interaction," *Phys. Rev. Lett.*, vol. 19, pp. 1312–1315, Dec 1967.

[39] J. B. McGuire, "Interacting fermions in one dimension. i. Repulsive potential," *Journal of Mathematical Physics*, vol. 6, no. 3, pp. 432–439, 1965.

[40] X.-W. Guan, M. T. Batchelor, and C. Lee, "Fermi gases in one dimension: From Bethe ansatz to experiments," *Rev. Mod. Phys.*, vol. 85, pp. 1633–1691, Nov 2013.

[41] B. Parades, A. Widera, V. Murg, O. Mandel, S. Fölling, I. Cirac, G. V. Shlyapnikov, T. W. Hänsch, and I. Bloch, "Tonks-Girardeau gas of ultracold atoms in an optical lattice," *Nature*, vol. 429, pp. 277–281, 2004.

[42] J.-B. Trebbia, J. Esteve, C. I. Westbrook, and I. Bouchoule, "Experimental evidence for the breakdown of a Hartree-Fock approach in a weakly interacting Bose gas," *Phys. Rev. Lett.*, vol. 97, p. 250403, Dec 2006.

[43] S. Gupta, K. W. Murch, K. L. Moore, T. P. Purdy, and D. M. Stamper-Kurn, "Bose-Einstein condensation in a circular waveguide," *Phys. Rev. Lett.*, vol. 95, p. 143201, Sep 2005.

[44] G. E. Marti, R. Olf, and D. M. Stamper-Kurn, "Collective excitation interferometry with a toroidal Bose-Einstein condensate," *Phys. Rev. A*, vol. 91, p. 013602, Jan 2015.

[45] B. E. Sherlock, M. Gildemeister, E. Owen, E. Nugent, and C. J. Foot, "Time-averaged adiabatic ring potential for ultracold atoms," *Phys. Rev. A*, vol. 83, p. 043408, Apr 2011.

[46] S. Hofferberth, I. Lesanovsky, B. Fischer, J. Verdu, and J. Schmiedmayer, "Radiofrequency-dressed-state potentials for neutral atoms," *Nature Physics*, vol. 2, pp. 710–716, 2006.

[47] J. A. Sauer, M. D. Barrett, and M. S. Chapman, "Storage ring for neutral atoms," *Phys. Rev. Lett.*, vol. 87, p. 270401, Dec 2001.

[48] S. Wu, W. Rooijakkers, P. Striehl, and M. Prentiss, "Bidirectional propagation of cold atoms in a stadium-shaped magnetic guide," *Phys. Rev. A*, vol. 70, p. 013409, Jul 2004.

[49] A. S. Arnold, C. S. Garvie, and E. Riis, "Large magnetic storage ring for Bose-Einstein condensates," *Phys. Rev. A*, vol. 73, p. 041606, Apr 2006.

[50] S. Eckel, J. G. Lee, F. Jendrzejewski, N. Murray, C. W. Clark, C. J. Lobb, W. D. Phillips, M. Edwards, and G. K. Campbell, "Hysteresis in a quantized superfluid atomtronic circuit," *Nature*, vol. 506, pp. 200–203, 2014.

[51] P. Massignan, M. Zaccanti, and G. M. Bruun, "Polarons, dressed molecules and itinerant ferromagnetism in ultracold Fermi gases," *Reports on Progress in Physics*, vol. 77, no. 3, p. 034401, 2014.

[52] F. N. Ünal, B. Hetényi, and M. O. Oktel, "Impurity coupled to an artificial magnetic field in a Fermi gas in a ring trap," *Phys. Rev. A*, vol. 91, p. 053625, May 2015.

[53] B. S. Shastry and B. Sutherland, "Twisted boundary conditions and effective mass in Heisenberg-Ising and Hubbard rings," *Phys. Rev. Lett.*, vol. 65, pp. 243–246, Jul 1990.

[54] M. Flicker and E. H. Lieb, "Delta-function Fermi gas with two-spin deviates," *Phys. Rev.*, vol. 161, pp. 179–188, Sep 1967.

[55] G. Lang, F. Hekking, and A. Minguzzi, "Dynamic structure factor and drag force in a one-dimensional strongly-interacting Bose gas at finite temperature," *arXiv:1503.08038*, 2015.

[56] F. N. Ünal, "Pairing in charged-neutral fermion mixtures under an artificial magnetic field," Master's thesis, Bilkent University, 2012.

[57] J. B. McGuire, "Interacting fermions in one dimension. II. Attractive potential," *Journal of Mathematical Physics*, vol. 7, no. 1, 1966.

[58] T. Jeltes, J. M. McNamara, W. Hogervorst, W. Vassen, V. Krachmalnicoff, M. Schellekens, A. Perrin, H. Chang, D. Boiron, A. Aspect, and C. I. Westbrook, "Comparison of the Hanbury Brown-Twiss effect for bosons and fermions," *Nature*, vol. 445, pp. 402–405, 2007.

[59] J. Friedel, "XIV. The distribution of electrons round impurities in monovalent metals," *The London, Edinburgh, and Dublin Philosophical Magazine and Journal of Science*, vol. 43, no. 337, pp. 153–189, 1952.

[60] J. Bardeen, L. N. Cooper, and J. R. Schrieffer, "Microscopic theory of superconductivity," *Phys. Rev.*, vol. 106, pp. 162–164, Apr 1957.

[61] P. W. Anderson, "The resonating valence bond state in La2CuO4 and superconductivity," *Science*, vol. 235, no. 4793, pp. 1196–1198, 1987.

[62] M. Inui, S. Doniach, P. J. Hirschfeld, and A. E. Ruckenstein, "Coexistence of antiferromagnetism and superconductivity in a mean-field theory of high-T_c superconductors," *Phys. Rev. B*, vol. 37, pp. 2320–2323, Feb 1988.

[63] G. Kotliar and J. Liu, "Superexchange mechanism and d -wave superconductivity," *Phys. Rev. B*, vol. 38, pp. 5142–5145, Sep 1988.

[64] C. Gros, D. Poilblanc, T. Rice, and F. Zhang, "Superconductivity in correlated wavefunctions," *Physica C: Superconductivity*, vol. 153, pp. 543 – 548, 1988.

[65] A. A. Abrikosov and L. P. Gor'kov *Sov. Phys. JETP*, vol. 12, p. 1243, 1961.

[66] T. Ando, Y. Matsumoto, and Y. Uemura, "Theory of Hall effect in a two-dimensional electron system," *Journal of the Physical Society of Japan*, vol. 39, no. 2, pp. 279–288, 1975.

[67] K. v. Klitzing, G. Dorda, and M. Pepper, "New method for high-accuracy determination of the fine-structure constant based on quantized Hall resistance," *Phys. Rev. Lett.*, vol. 45, pp. 494–497, Aug 1980.

[68] R. B. Laughlin, "Quantized Hall conductivity in two dimensions," *Phys. Rev. B*, vol. 23, pp. 5632–5633, May 1981.

[69] D. J. Thouless, "Quantization of particle transport," *Phys. Rev. B*, vol. 27, pp. 6083–6087, May 1983.

[70] B. J. Ramshaw, S. E. Sebastian, R. D. McDonald, J. Day, B. S. Tan, Z. Zhu, J. B. Betts, R. Liang, D. A. Bonn, W. N. Hardy, and N. Harrison, "Quasiparticle mass enhancement approaching optimal doping in a high-Tc superconductor," *Science*, vol. 348, no. 6232, pp. 317–320, 2015.

[71] J. R. Abo-Shaeer, C. Raman, J. M. Vogels, and W. Ketterle, "Observation of vortex lattices in Bose-Einstein condensates," *Science*, vol. 292, no. 5516, pp. 476–479, 2001.

[72] E. Hodby, G. Hechenblaikner, S. A. Hopkins, O. M. Maragò, and C. J. Foot, "Vortex nucleation in Bose-Einstein condensates in an oblate, purely magnetic potential," *Phys. Rev. Lett.*, vol. 88, p. 010405, Dec 2001.

[73] K. W. Madison, F. Chevy, W. Wohlleben, and J. Dalibard, "Vortex formation in a stirred Bose-Einstein condensate," *Phys. Rev. Lett.*, vol. 84, pp. 806–809, Jan 2000.

[74] A. L. Gaunt, T. F. Schmidutz, I. Gotlibovych, R. P. Smith, and Z. Hadzibabic, "Bose-Einstein condensation of atoms in a uniform potential," *Phys. Rev. Lett.*, vol. 110, p. 200406, May 2013.

[75] F. N. Ünal and M. O. Oktel, "Pairing of fermions with unequal effective charges in an artificial magnetic field," *Phys. Rev. Lett.*, vol. 116, p. 045305, Jan 2016.

[76] G. Möller and N. R. Cooper, "Density waves and supersolidity in rapidly rotating atomic fermi gases," *Phys. Rev. Lett.*, vol. 99, p. 190409, Nov 2007.

[77] H. Zhai and T.-L. Ho, "Critical rotational frequency for superfluid fermionic gases across a feshbach resonance," *Phys. Rev. Lett.*, vol. 97, p. 180414, Nov 2006.

[78] V. Gurarie and L. Radzihovsky, "Resonantly paired fermionic superfluids," *Annals of Physics*, vol. 322, no. 1, pp. 2 – 119, 2007. January Special Issue 2007.

[79] V. L. Ginzburg and L. D. Landau *Zh. Eksp. Teor. Fiz.*, vol. 20, p. 1064, 1950.

[80] M. Rasolt and Z. Tesănović, "Theoretical aspects of superconductivity in very high magnetic fields," *Rev. Mod. Phys.*, vol. 64, pp. 709–754, Jul 1992.

[81] L. W. Gruenberg and L. Gunther, "Effect of orbital quantization on the critical field of type-II superconductors," *Phys. Rev.*, vol. 176, pp. 606–613, Dec 1968.

[82] M. V. Hosseini and M. Zareyan, "Model of an exotic chiral superconducting phase in a graphene bilayer," *Phys. Rev. Lett.*, vol. 108, p. 147001, Apr 2012.

[83] A. Sedrakian and U. Lombardo, "Thermodynamics of a $n - p$ condensate in asymmetric nuclear matter," *Phys. Rev. Lett.*, vol. 84, pp. 602–605, Jan 2000.

[84] P. Fulde, "Cooper pair breaking," *Modern Physics Letters B*, vol. 24, no. 26, pp. 2601–2624, 2010.

[85] M. Aidelsburger, M. Lohse, C. Schweizer, M. Atala, J. T. Barreiro, S. Nascimbène, N. R. Cooper, I. Bloch, and N. Goldman, "Measuring the Chern number of Hofstadter bands with ultracold bosonic atoms," *Nature Physics*, vol. 11, p. 162, 2015.

[86] M. Atala, M. Aidelsburger, M. Lohse, J. T. Barreiro, B. Paredes, and I. Bloch, "Observation of chiral currents with ultracold atoms in bosonic ladders," *Nature*, vol. 10, pp. 588–593, 2014.

[87] M. Z. Hasan and C. L. Kane, "*Colloquium* : Topological insulators," *Rev. Mod. Phys.*, vol. 82, pp. 3045–3067, Nov 2010.

[88] B. Douçot, V. Pasquier, and V. Rivasseau, eds., *The Quantum* H*all Effect, Poincaré Seminar 2004*. Birkhäuser Basel, 2005.

[89] M. S. Foster, V. Gurarie, M. Dzero, and E. A. Yuzbashyan, "Quench-induced Floquet topological p-wave superfluids," *Phys. Rev. Lett.*, vol. 113, p. 076403, Aug 2014.

[90] L. DAlessio and M. Rigol, "Dynamical preparation of Floquet Chern insulators," *Nature Communications*, vol. 6, p. 8336, 2014.

[91] M. D. Caio, N. R. Cooper, and M. J. Bhaseen, "Quantum quenches in Chern insulators," *Phys. Rev. Lett.*, vol. 115, p. 236403, Dec 2015.

[92] J. H. Wilson, J. C. W. Song, and G. Refael, "Remnant geometric Hall response in a quantum quench," *Phys. Rev. Lett.*, vol. 117, p. 235302, Nov 2016.

[93] P. Wang, M. Schmitt, and S. Kehrein, "Universal nonanalytic behavior of the Hall conductance in a Chern insulator at the topologically driven nonequilibrium phase transition," *Phys. Rev. B*, vol. 93, p. 085134, Feb 2016.

[94] Y. Hu, P. Zoller, and J. C. Budich, "Dynamical buildup of a quantized Hall response from nontopological states," *Phys. Rev. Lett.*, vol. 117, p. 126803, Sep 2016.

[95] H. Dehghani, T. Oka, and A. Mitra, "Out-of-equilibrium electrons and the Hall conductance of a Floquet topological insulator," *Phys. Rev. B*, vol. 91, p. 155422, Apr 2015.

[96] F. N. Ünal, E. J. Mueller, and M. O. Oktel, "Nonequilibrium fractional Hall response after a topological quench," *Phys. Rev. A*, vol. 94, p. 053604, Nov 2016.

[97] D. J. Thouless, M. Kohmoto, M. P. Nightingale, and M. den Nijs, "Quantized Hall conductance in a two-dimensional periodic potential," *Phys. Rev. Lett.*, vol. 49, pp. 405–408, Aug 1982.

[98] M. D. Caio, N. R. Cooper, and M. J. Bhaseen, "Hall response and edge current dynamics in Chern insulators out of equilibrium," *Phys. Rev. B*, vol. 94, p. 155104, Oct 2016.

[99] H. M. Price and N. R. Cooper, "Mapping the Berry curvature from semiclassical dynamics in optical lattices," *Phys. Rev. A*, vol. 85, p. 033620, Mar 2012.

[100] N. Goldman, G. Jotzu, M. Messer, F. Grg, R. Desbuquois, and T. Esslinger, "Creating topological interfaces and detecting chiral edge modes in a 2D optical lattice," *arXiv:1606.00015*, 2016.

[101] M. R. Matthews, B. P. Anderson, P. C. Haljan, D. S. Hall, C. E. Wieman, and E. A. Cornell, "Vortices in a Bose-Einstein condensate," *Phys. Rev. Lett.*, vol. 83, pp. 2498–2501, Sep 1999.

[102] A. P. Chikkatur, A. Görlitz, D. M. Stamper-Kurn, S. Inouye, S. Gupta, and W. Ketterle, "Suppression and enhancement of impurity scattering in a Bose-Einstein condensate," *Phys. Rev. Lett.*, vol. 85, pp. 483–486, Jul 2000.

[103] K. C. Wright, L. S. Leslie, and N. P. Bigelow, "Raman coupling of Zeeman sublevels in an alkali-metal Bose-Einstein condensate," *Phys. Rev. A*, vol. 78, p. 053412, Nov 2008.

[104] S. Keßler and F. Marquardt, "Single-site-resolved measurement of the current statistics in optical lattices," *Phys. Rev. A*, vol. 89, p. 061601, Jun 2014.

Appendix A

Publications in SCI journals

[1] F. Nur Ünal and Erich J. Mueller, *Cooling Quantum Gases with Entropy Localization*, New Journal of Physics (under review), arXiv:1604.04277 (2016).

[2] F. Nur Ünal, Erich J. Mueller, and M. Ö. Oktel, *Nonequilibrium fractional Hall response after a topological quench*, Phys. Rev. A 94, 053604 (2016).

[3] F. Nur Ünal and M. Ö. Oktel, *Pairing of Fermions with Unequal Effective Charges in an Artificial Magnetic Field*, Phys. Rev. Lett. 116, 045305 (2016).

[4] F. Ylmaz, F. Nur Ünal, and M. Ö. Oktel, *Evolution of the Hofstadter butterfly in a tunable optical lattice*, Phys. Rev. A 91, 063628 (2015).

[5] F. Nur Ünal, B. Hetenyi, and M. Ö. Oktel, *Impurity coupled to an artificial magnetic field in a Fermi gas in a ring trap*, Phys. Rev. A 91, 053625 (2015).